nature portfolio

https://doi.org/10.1038/s41586-024-07339-7

Supplementary information

Growth of diamond in liquid metal at 1 atm pressure

In the format provided by the authors and unedited

Supplementary Information

Growth of diamond in liquid metal at 1 atmosphere pressure

Yan Gong[1,2], Da Luo[1], Myeonggi Choe[1,3], Yongchul Kim[1,2], Babu Ram[1], Mohammad Zafari[1], Won Kyung Seong[1]*, Pavel Bakharev[1], Meihui Wang[1], In Kee Park[2], Seulyi Lee[4], Tae Joo Shin[5], Zonghoon Lee[1,3], Geunsik Lee[2], Rodney S. Ruoff[1,2,3,6]**

1.Center for Multidimensional Carbon Materials (CMCM), Institute for Basic Science (IBS), Ulsan 44919, Republic of Korea.

2.Department of Chemistry, Ulsan National Institute of Science and Technology (UNIST), Ulsan 44919, Republic of Korea.

3.Department of Materials Science and Engineering, Ulsan National Institute of Science and Technology (UNIST), Ulsan 44919, Republic of Korea.

4. UNIST Central Research Facilities (UCRF), Ulsan National University of Science and Technology (UNIST), Ulsan 44919, Republic of Korea.

5. Graduate School of Semiconductor Materials and Devices Engineering, Ulsan National University of Science and Technology (UNIST), Ulsan 44919, Republic of Korea.

6.School of Energy and Chemical Engineering, Ulsan National Institute of Science and Technology (UNIST), Ulsan 44919, Republic of Korea.

E-mail: ruofflab@gmail.com, rsruoff@ibs.re.kr, luodarhoda@gmail.com, one2rang@gmail.com

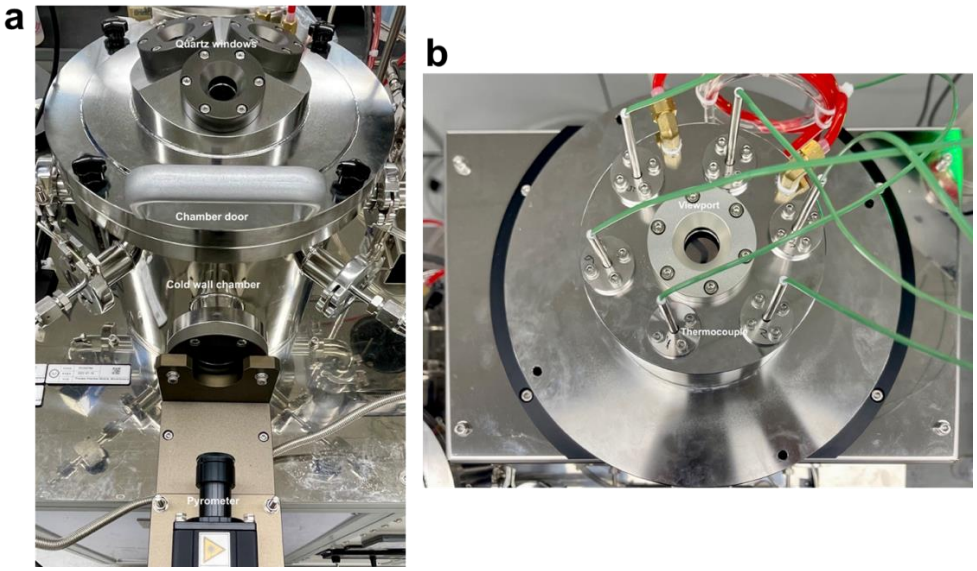

Figure S1. Photographs of the (a) home-built cold-wall system for diamond growth, and the (b) home-built thermocouple setup.

A cold wall chamber with a chamber volume of 9 L and three quartz windows on the chamber door for in-situ observation was used (Fig. S1a). The chamber's base vacuum (10^{-3} Torr) was achieved using a rotary pump (Edwards Vacuum Co., E2M28FX). The Joule heating method for diamond growth employs a water-cooled electrode and graphite crucible, with temperature control of the crucible achieved using a pyrometer (Sensor Therm GmbH, Metis M313) with a feedback loop. The ~1 mm diameter laser spot of the pyrometer was focused on the center of the outside part of the side of the graphite crucible. The pyrometer utilized a 1.27-micrometer infrared wavelength and was mounted on the lateral quartz viewport of the chamber.

For measuring the temperatures in several different locations in the liquid metal, six R-type thermocouples were used as shown (Fig. S1b). These thermocouples were fixed on the cold wall-type chamber door, with a central viewport ensuring accurate positioning between the liquid metal and thermocouples. The temperature measurement region of the R-type thermocouples is sheathed with an alumina tube to prevent reactions with the liquid metal at the point of contact. The sealing of the R-type thermocouples in the chamber door was done with stainless steel tubes. The temperature of the R-type thermocouples was logged using a temperature data logger (Graphtec

Corp., GL240) during the experiments.

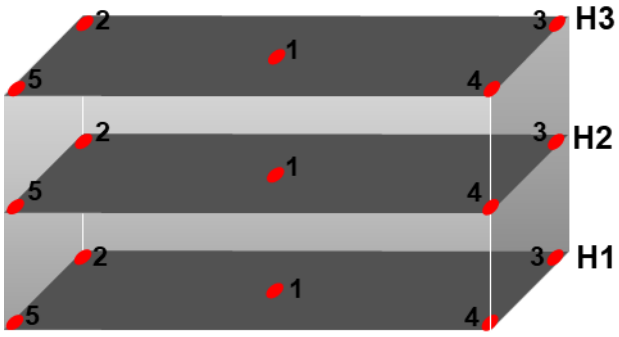

Figure S2. Scheme showing the different regions (positions) at which temperatures were measured by inserting alumina-sheathed thermocouples into the liquid metal (77.75/11.0/11.0/0.25 mix (atomic percentages) of Ga/Ni/Fe/Si).

Table S1. Temperatures at the 15 positions in Fig. S2 measured with inserted thermocouples when the 'pyrometer temperature' reads 1175 °C.

Positions	H1	H2	H3
1	1025 °C	1006 °C	978 °C
2	1084 °C	1023 °C	982 °C
3	1081 °C	1020 °C	985 °C
4	1086 °C	1025 °C	980 °C
5	1082 °C	1018 °C	978 °C

Table S2. Temperatures at position H1-1 measured by the thermocouple for different 'pyrometer temperatures'.

Pyrometer temperature	1165 °C	1175 °C	1190 °C	1200 °C
Thermocouple temperature	1008 °C	1022 °C	1042 °C	1060 °C

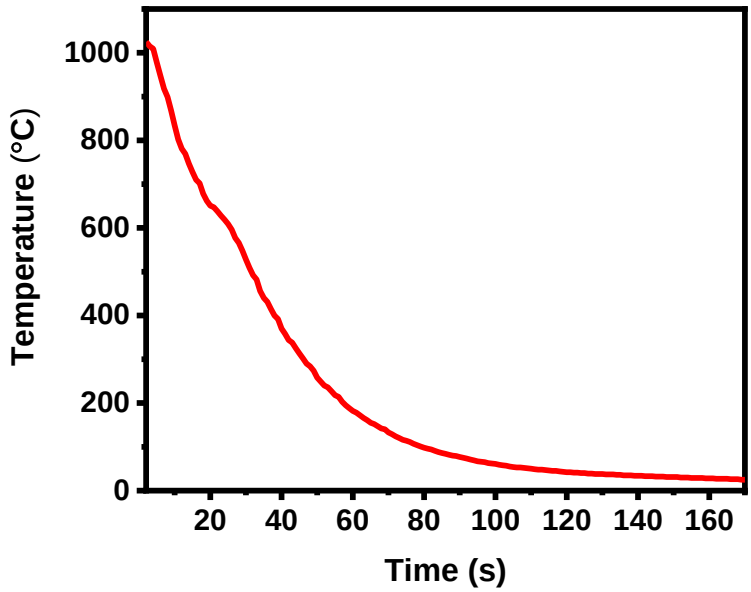

Figure S3. 'Quenching' experiments. The liquid metal in the graphite crucible was rapidly cooled ('quenched') by turning off the current (after the current stabilized, with pyrometer reading 1175 °C which was found to be after about 5 minutes). The temperature-time curve was recorded by measuring the temperature with a thermocouple positioned at H1-1 (as shown in Fig. S2) in the liquid metal (77.75/11.0/11.0/0.25 mix (atomic percentages) of Ga/Ni/Fe/Si) under 760 Torr of methane/hydrogen (1/20 molar ratio).

When the pyrometer reads 1175 °C, the thermocouple positioned at H1-1 reads 1025 °C. The liquid metal cools to 25 °C in about 167 seconds, and (in Kelvin units) to one half of the initial (absolute) temperature of 1025 °C (1298 K), thus to 376 °C (649 K) in about 40 seconds.

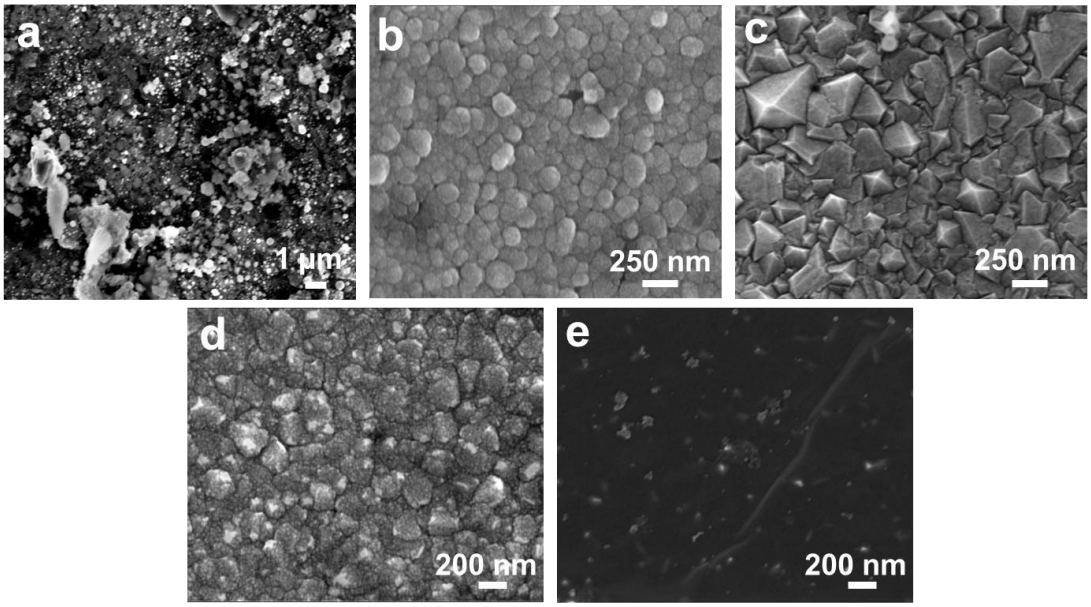

Figure S4. SEM images of the center region of 5 different solidified liquid metal pieces after growths at different temperatures. All growth runs: 760 Torr, 150 min, 0.25 at% Si, 11.00 at% Ni, 11.00 at% Fe, 77.75 at% Ga. (a) 1155 °C. (b) 1165 °C. (c) 1175 °C. (d) 1190 °C. (e) 1200 °C.

When the growth temperature was 1155 °C, amorphous carbon and silica were observed to be formed on the surface of the liquid metal piece. When the temperature was increased to 1200 °C, a large amount of graphite was found to be deposited on the metal surface. We found diamonds can be grown at the bottom of the crucible, most typically in its central region, in the temperature range between 1165 °C and 1190 °C. For 1165 °C the diamond particle morphology tends to be round, and some amorphous carbon was observed. For 1175 °C, diamond facets were observed, and the size of diamond crystals increased. For 1190 °C much more graphitic carbon formed along with the growth of diamond crystals.

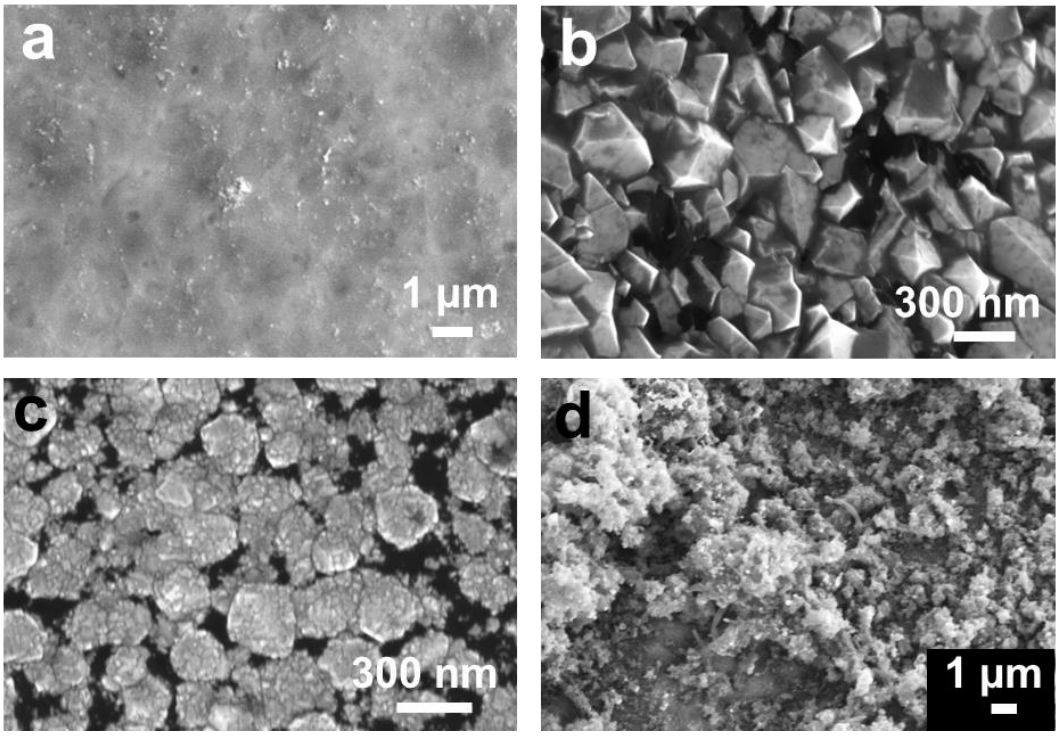

Figure S5. SEM images showing the diamond found at the center regions of the bottom of the solidified liquid metal piece for different concentrations of silicon. All growth runs: 760 Torr, 1175 °C, 150 min with 11.00 at% Ni and Fe each. The silicon concentrations were (a) 0.00 at%, (no diamond was found) (b) 0.25 at%, (c) 0.50 at%, and (d) 1.00 at%.

We found silicon plays an important role for diamond growth and that the growth of diamond is sensitive to the concentration of the added silicon. If there was no silicon added, only graphite was formed (Fig. S5a). Adding 0.25 at% silicon leads to the growth of diamonds on the surface of the liquid metal piece (Fig. S5b). With more silicon added, the nucleation density of diamonds greatly increased while the crystal size decreased (Fig. S5c). For 1.00 at% Si, SiO_2 was found to cover the entire metal surface and diamonds were not observed (Fig. S5d).

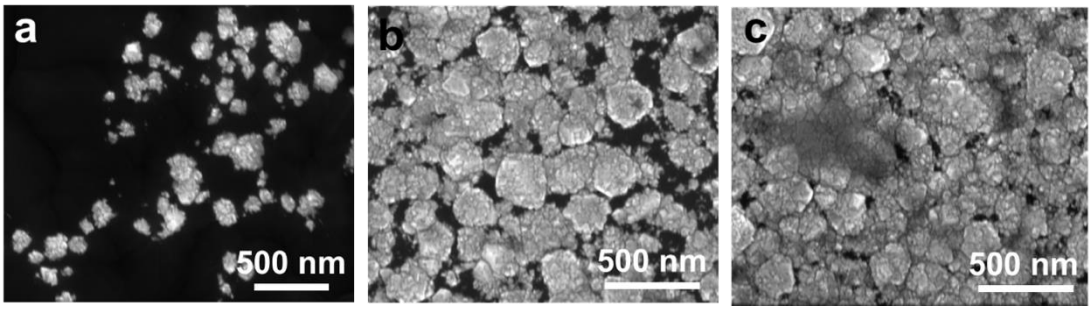

Figure S6. SEM images showing the growth at the center regions of the solidified liquid metal piece for different growth times. All growth runs: 760 Torr, 1175 °C, 0.50 at% Si, 11.00 at% Ni, 11.00 at% Fe, 77.50 at% Ga. (a) 40 min. (b) 150 min. (c) 210 min.

For 0.50 at% Si added, diamond crystals of sizes of ~20 nm were formed, and they were observed to form aggregates (Fig. S6a). Increasing the growth time does not lead to the increase of the size of the tiny diamond crystals, while both the density and size of the aggregates increase (Fig. S6b-c). This suggests that nucleation density of diamond crystals is strongly correlated with the amount of silicon in the liquid metal alloy.

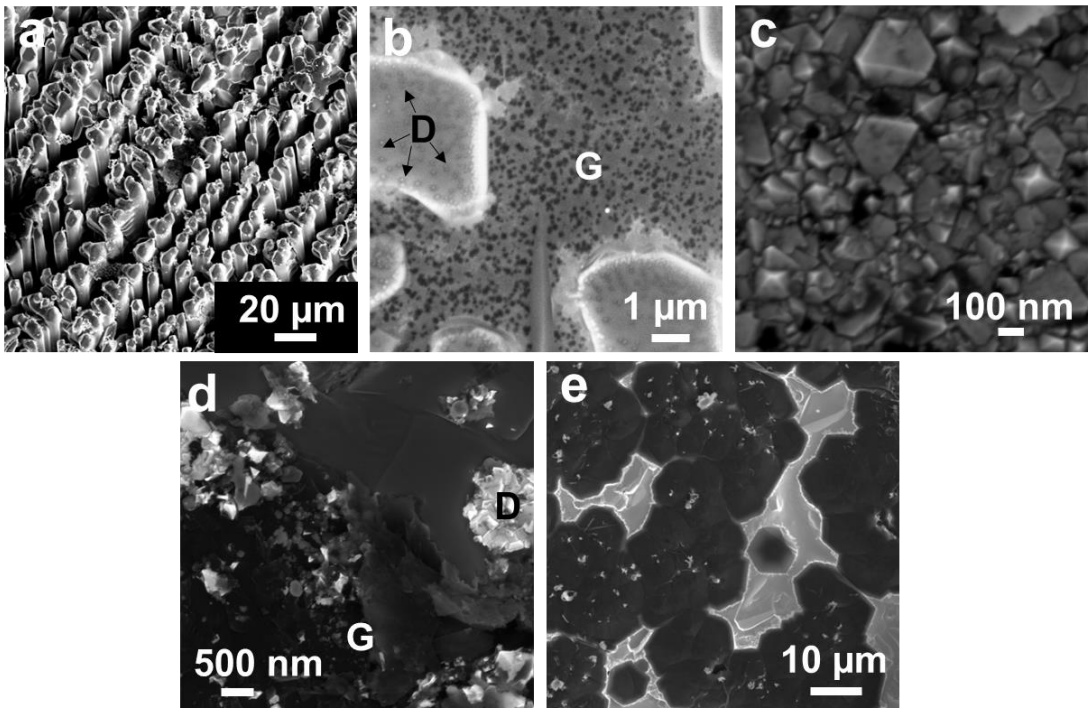

Figure S7. SEM images showing the growth at the center regions of the solidified liquid metal piece with different concentrations of nickel added. All growth runs: 760 Torr, 1175 °C, 150 min. Concentrations of Fe and Si are fixed at 11.00 at% and 0.25 at%, respectively. The concentrations of nickel were (a) 0.00 at%, (b) 6.00 at%, (c) 11.00 at%, (d) 18.00 at%, and (e) 25.00 at%.

When Ni was not included in the liquid metal alloy, we did not find any carbon deposited on the solidified liquid metal piece (Fig. S7a). When 6.00 at% of Ni was added, some multilayer graphene islands together with many diamond crystals of ~100 nm size were observed on the surface of the solidified liquid metal piece (Fig. S7b). For 11 at% of Ni (we note this is our optimal and typical growth condition for growing diamonds), diamond crystals with obvious and sharp facets were grown (Fig. S7c). For 18.00 at% Ni, we found most regions were coated by graphite structures, while a few regions show diamond crystals (Fig. S7d). For 25.00 at% Ni, only graphite was found on the surface of the solidified liquid metal piece, i.e., we did not find diamonds for this growth condition (Fig. S7e). (It should be noted that the concentration of gallium (in at %) is also being varied in this parametric study, for each Ni concentration used.)

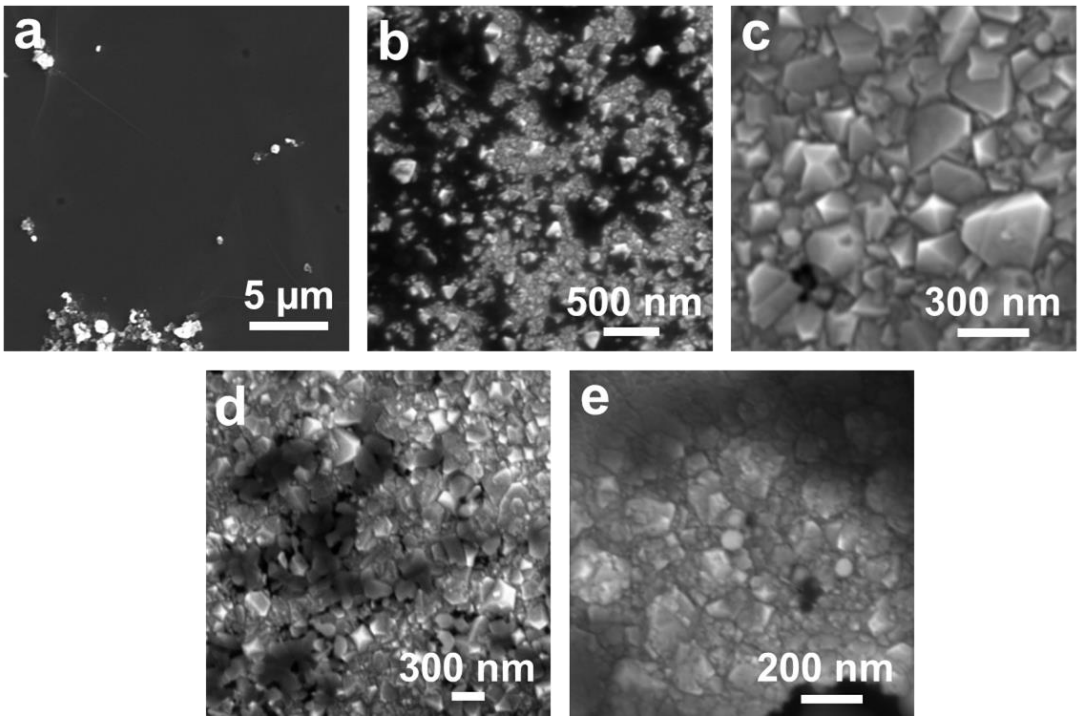

Figure S8. SEM images showing the growth at the center regions of the solidified liquid metal piece with different concentrations of iron added. All growth runs: 760 Torr, 1175 °C, 150 min. Concentrations of Ni and Si are fixed at and 11.00 at% and 0.25 at%, respectively. The concentrations of iron were (a) 0.00 at%, (b) 6.00 at%, (c) 11.00 at%, (d) 18.00 at%, and (e) 25.00 at%.

When Fe was not included in the liquid metal alloy, only graphite (almost continuous graphite film) was observed on the surface of the solidified liquid metal piece (Fig. S8a).

For 6.00 at% Fe we found the growth of graphite was significantly suppressed and diamond crystals were observed in certain regions (Fig. S8b). For 11.00 at% Fe, (we note this is the optimal and typical growth condition for growing diamonds), diamond crystals with obvious and sharp facets were grown (Fig. S8c). Further increasing the concentrations of Fe leads to the growth of diamond crystals (Fig. S8d-e) of smaller sizes. (It should be noted that the concentration of gallium (in at %) is also being varied in this parametric study, for each Fe concentration used.)

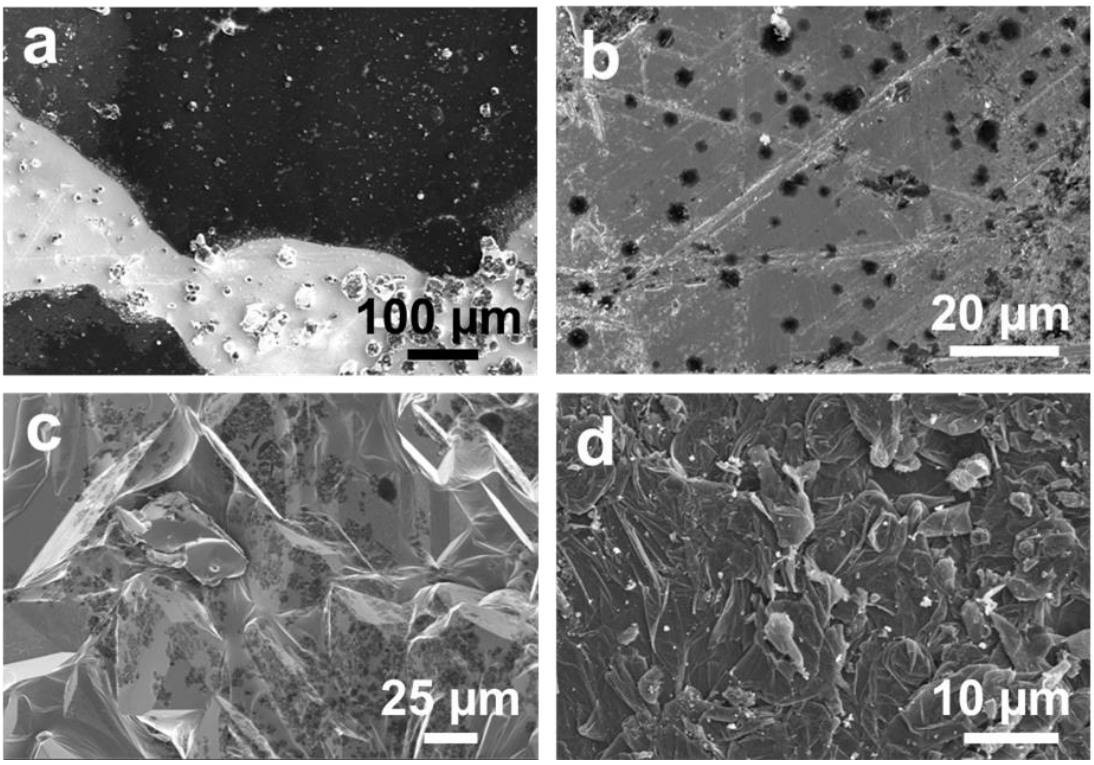

Figure S9. SEM images showing the growths found at the center regions of the solidified liquid metal piece by using molten liquid metals of different compositions. All growth runs: 760 Torr, 1175 °C, 150 min. (a) Pure Ga. (b) Ga with 0.25 at% of silicon added. (c) Ga with 11 at% of Fe added. (d) Ga with 11 at% Ni added.

When pure gallium was used for the growth, we found thin layers of graphite formed on certain regions on the surface of the solidified liquid metal piece (Fig. S9a). For 0.25 at% Si we found multilayer graphene or graphite islands (regions in black in Fig. S9b) of a very low surface coverage grown on the metal surface. For 11.00 at% Fe thin graphitic structures (regions in black in Fig. S9c) were found formed on some regions. For 11.00 at% Ni we found very thick graphite was formed and covered the entire metal surface (Fig. S9d). The results above suggest that Ni added to Ga is likely to gather larger amounts of carbon to or into the liquid metal alloy surface, while both Si and Fe added to the Ga seem to suppress the formation of graphitic carbon on the liquid metal surface, compared to the growth by using pure Ga.

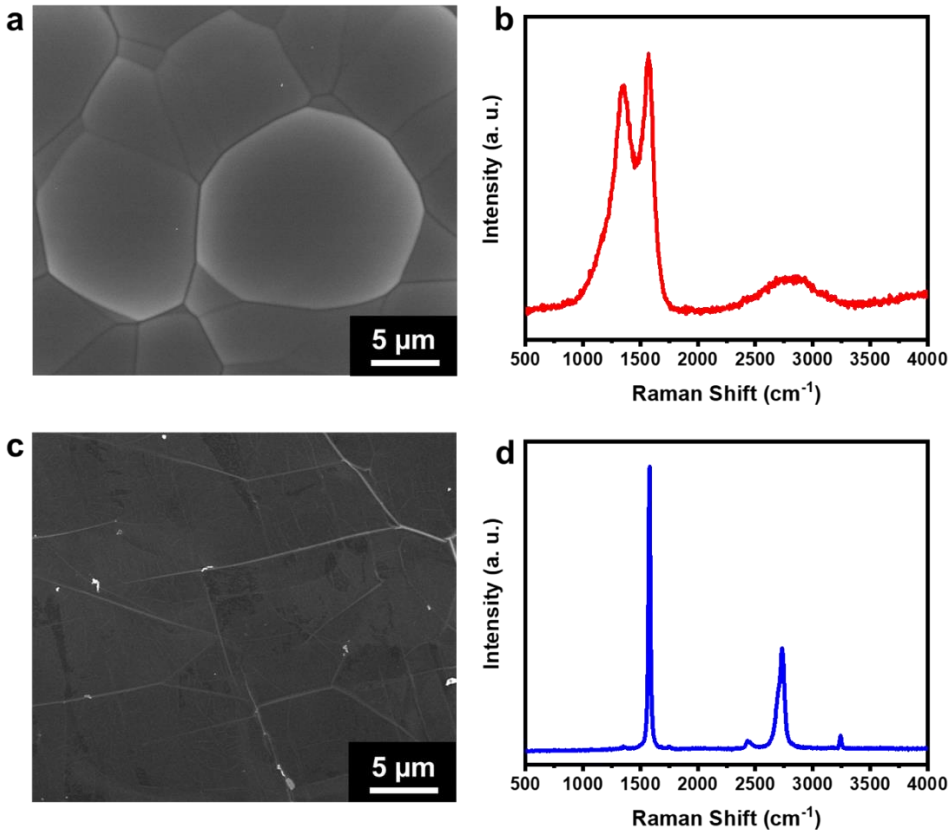

Figure S10. SEM images and Raman spectra of the growths with no H_2 present. (a, b) The growth with only CH_4 present. (c, d) The growth with 5/100 CH_4/Ar. Experiment parameters: 1175 ºC, 760 Torr, 150 min, 0.25 at% Si, 11.00 at% Ni, 11.00 at% Fe, 77.75 at% Ga.

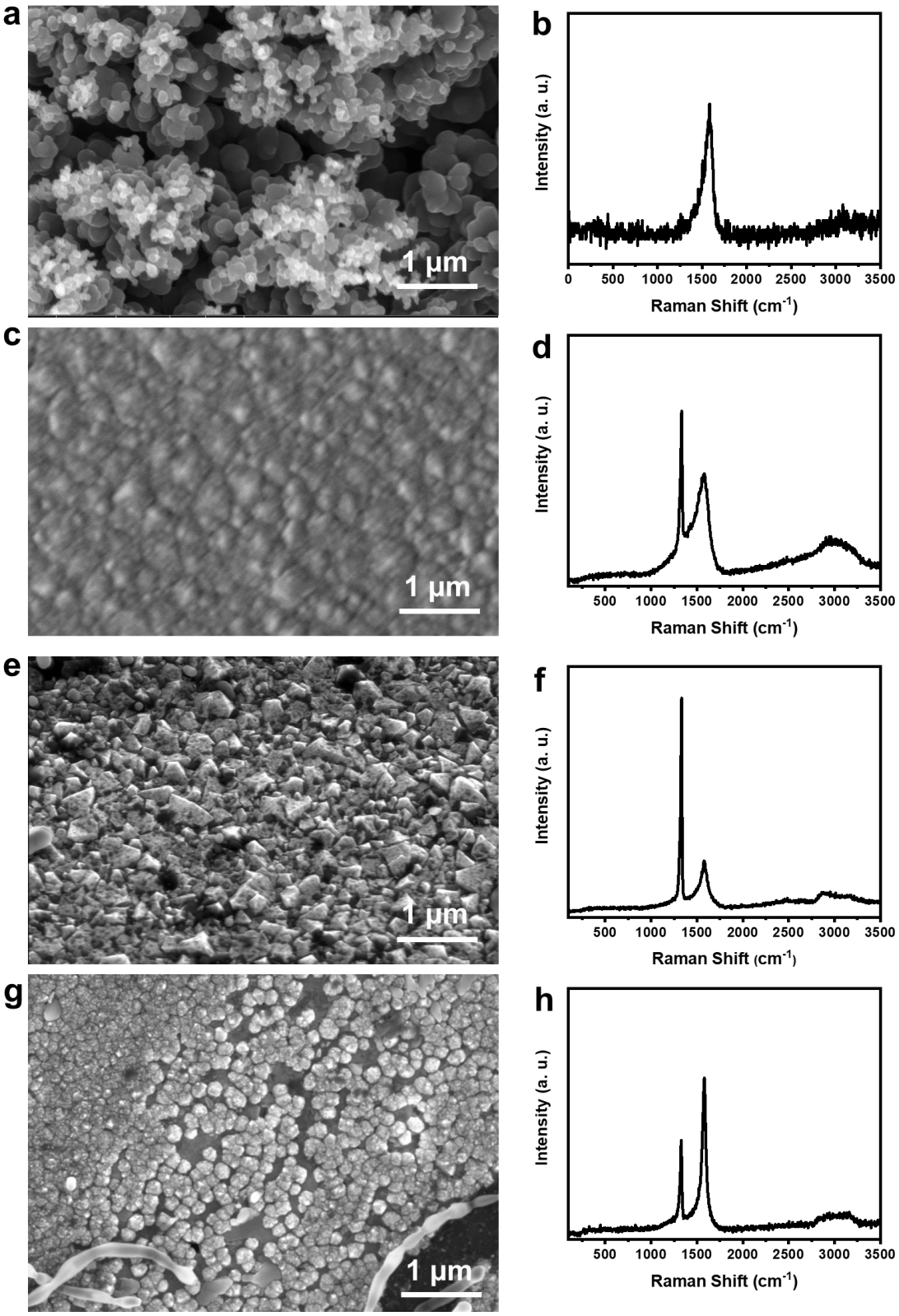

Figure S11. SEM images and Raman spectra of the growths with different ratios of CH_4 /H_2. (a, b) 1/100 CH_4 /H_2. (c, d) 2.5/100 CH_4 /H_2. (e, f) 10/100 CH_4 /H_2. (g, h) 20/100 CH_4 /H_2. Experiment parameters: 1175 ºC, 760 Torr, 150 min; 0.25 at% Si, 11.00 at% Ni, 11.00 at% Fe, 77.75 at% Ga.

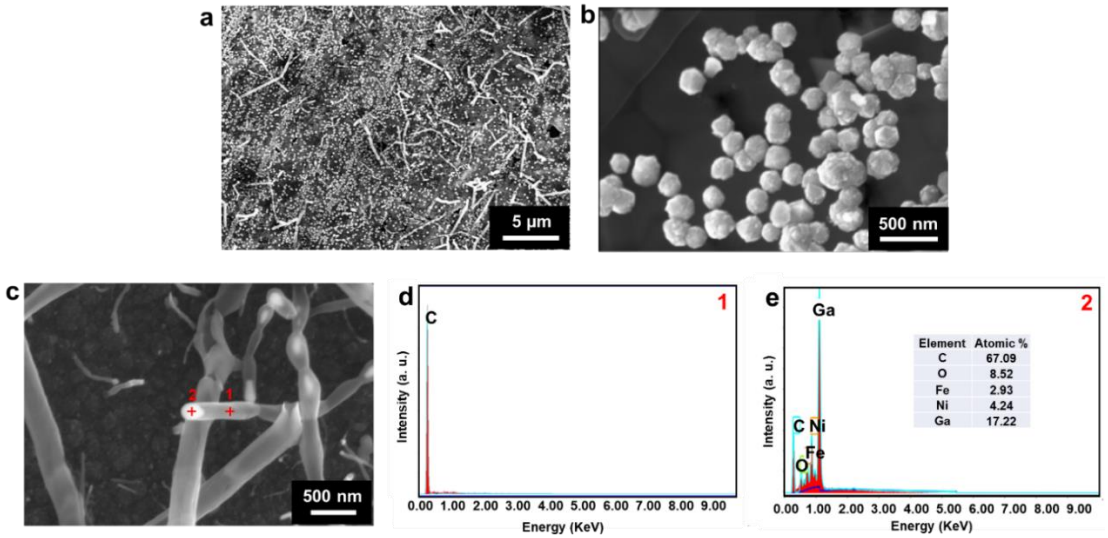

Figure S12. SEM images and EDS analysis of the growth using 20/100 CH_4/H_2. (a) Low magnification SEM image of diamond crystals and carbon fibers grown on metal alloy piece. (b) High magnification SEM image of diamond crystals grown on metal alloy piece. (c) High magnification SEM image of carbon fiber. EDS analysis of regions 1 (d) and 2 (e) of carbon fibers in (c).

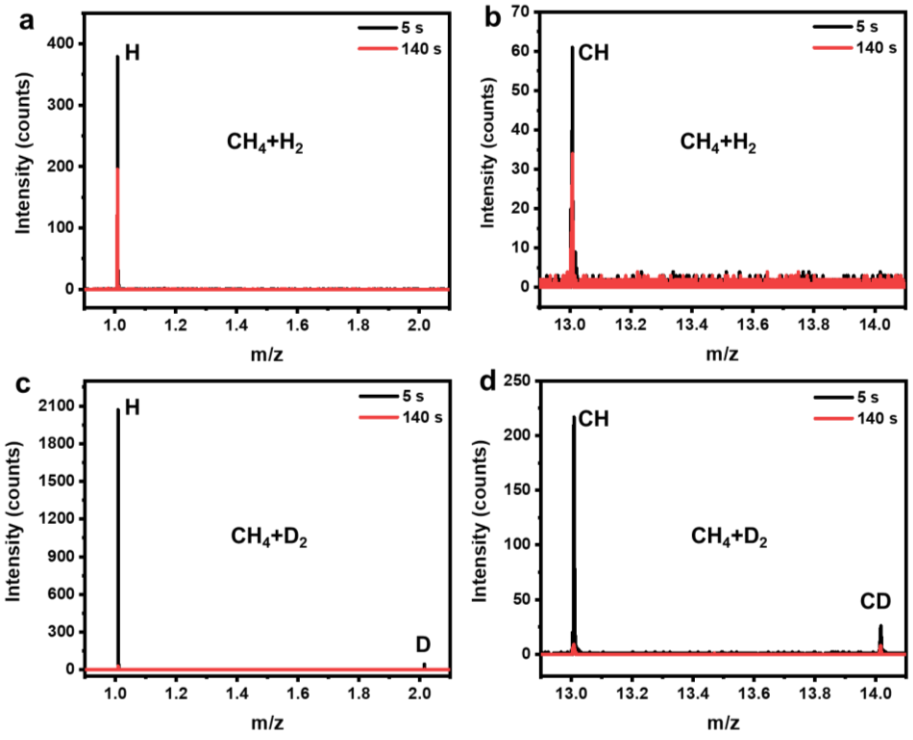

Figure S13. ToF-SIMS surface spectra of the D-labeled as-grown diamond film (solidified liquid metal piece from the run with CH_4/ D_2 (5/100)) compared to a typical run (of CH_4/ H_2 (5/100)). H peak (a) and CH peak (b) of the as-grown diamond film of CH_4/ H_2 after 5s and 140s sputtering. The peaks of H and D (c), and CH and CD (d) of the as-grown diamond film of CH_4/ D_2 after 5s and 140s sputtering.

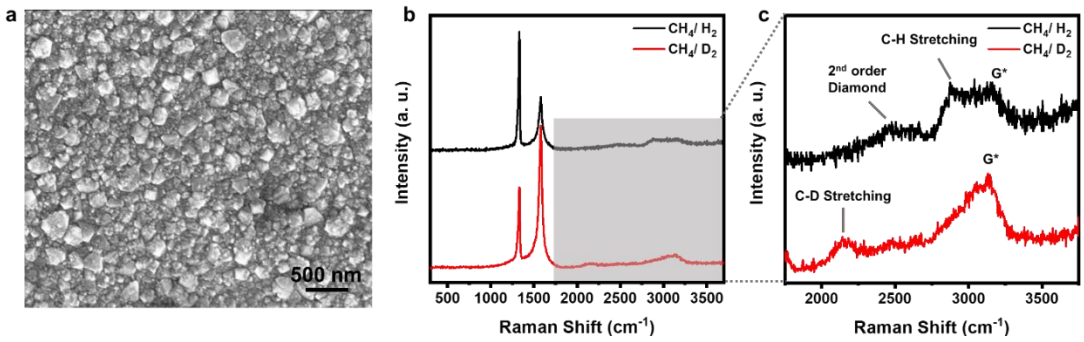

Figure S14. SEM image and UV Raman analysis of the D-labeled as-grown diamond film. (a) SEM image. (b) UV Raman spectra of D-labeled as-grown diamond film compared to the typical one generated by our optimized run with normal methane and hydrogen gases. (c) An expanded view of (b) that shows the typical diamond C-H stretching peak compared to D-labeled diamond.

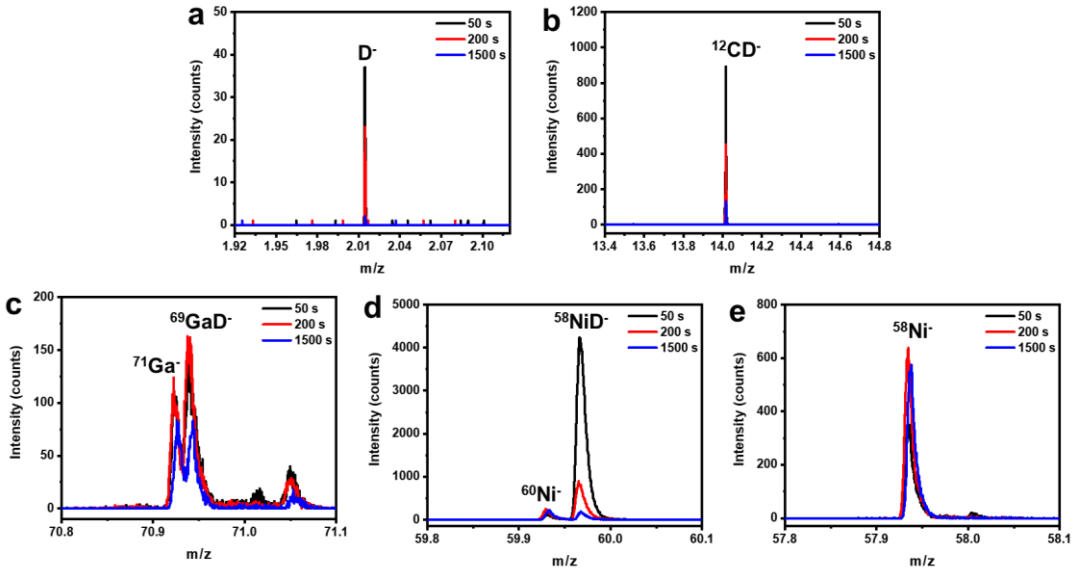

Figure S15. ToF-SIMS surface spectra of the solidified liquid metal for the CH_4/ D_2 (5/100) run at 50, 200, and 1500 seconds. (a) D^- peaks. (b) $^{12}CD^-$ peaks. (c) $^{71}Ga^-$ and $^{69}GaD^-$ peaks. (d) $^{60}Ni^-$ and $^{58}NiD^-$ peaks. (e) $^{58}Ni^-$ peaks.

We studied the role of H_2 in Fig. S10-15 as shown above.

i) We did two growth experiments with no hydrogen present, one with pure methane and the other with methane diluted in argon. With 1 atm pure CH_4 (with a slight flow through our growth chamber, i.e., not a closed volume) we found thick graphite grown everywhere on the solidified liquid metal piece (Fig. S10a) and no diamond grew. An intense Raman D band observed in the Raman spectrum shows

the graphite was defective (Fig. S10b). For CH_4/Ar of 5/100, we found a very high-quality thick graphite film having no Raman D band (Fig. S10c-d) on all the solidified liquid metal piece surface, and no diamond grew. These 2 runs suggest that H_2 is needed to grow diamond under our current 'optimal' conditions of the LM mixture of Ga/Fe/Ni/Si (77.75/11/11/0.25 atomic percentages).

ii) Growth experiments with CH_4/H_2 of 1/100, 2.5/100, 10/100 and 20/100 were done to further study the role of hydrogen in diamond growth. Excepting 1/100 CH_4/H_2, the 2.5/100, 10/100 and 20/100 gas mixtures all led to diamond formation on the solidified liquid metal surface. For CH_4/H_2 of 1/100, only amorphous carbon was found on the solidified liquid metal surface (Fig. S11a-b). For CH_4/H_2 of 2.5/100 diamonds with small crystal size were found. Facets were not clearly exposed, and the quality is 'not good' (Fig. S11c-d). For CH_4/H_2 of 10/100, the morphology of diamonds is very similar to those obtained in our typical runs (5/100 CH_4/H_2) (Fig. S11e-f). For CH_4/H_2 of 20/100, "round ball" shape diamond crystals were grown, with the growth of by-product carbon fibers (Fig. S11g-f, S12).

Our results i) and ii) suggest that appropriate amounts of H_2 (100/2.5 ~ 100/20 of H_2/CH_4 molar ratio; literally volume ratio as we assume ideal gas to obtain mol percentages) is critical for the growth of diamonds. Also: The H_2/CH_4 should not be *larger* than 100/2.5; when it is, diamond does not grow, likely due to insufficient carbon in the source gas for the growth.

We did a growth by replacing H_2 with D_2 and obtained ToF-SIMS spectra from the as-grown diamonds. We note that for the diamonds grown by using CH_4/ H_2, there is no peak at *m/z* of 2 (for H_2^-; that is 2.01565 amu) and 14 (for CH_2^-; that is 14.01565 amu) (Fig. S13a-b). For the diamonds grown using CH_4/D_2, peaks at *m/z* of 2 and 14 were observed (Fig. S13c-d) and assigned to D^- (2.014102 amu) and CD^- (14.014102 amu). The intensity of these two peaks dramatically decreased after sputtering for 140s (reaching a depth of 14 nm), suggesting that D was mainly present on the diamond surfaces, i.e., the diamond surfaces were hydrogenated. We note that the very weak (but not zero) intensity of the CD^- peak at the depth of 14 nm is very likely suggesting that there is hydrogen (here, deuterium) present at the grain boundaries between diamond

grains, since our as-grown diamond film is polycrystalline.

The Raman spectrum (Fig. S14) of the as-grown diamond film by using CH_4/ H_2 in our standard runs shows a peak at 2878 cm^{-1} that we assign as a C-H stretching peak; this peak is redshifted to 2150 cm^{-1} for the diamond film that is grown by using CH_4/D_2, corresponding to the peak frequency for C-D stretching[1,2]. Our Raman studies thus suggest that our as-grown diamond surfaces are terminated by hydrogen.

We delaminated (by using a double-side copper tape) the as-grown diamond film from the D_2/CH_4 growth (discussed above) and obtained ToF-SIMS data from the diamond-grown region on the solidified liquid metal piece. The data show the ions D^- (2.014102 amu), $^{12}CD^-$ (14.014102 amu), $^{69}GaD^-$ (70.939675 amu), $^{58}NiD^-$ (59.949444 amu) present in the solidified liquid metal piece, with intensities decreasing from a depth of 10 nm (sputtering for 50s), to depths of 40 nm (sputtering for 200s) and 300 nm (sputtering for 1500s) (Fig. S15a-d). We note that the mass of $^{56}FeD^-$ (57.949037 amu) is very close to $^{58}Ni^-$ (57.935342 amu) and thus we cannot assign its possible presence.

In summary, our studies to date suggest hydrogen should be introduced to grow diamond by our method. Our as-grown diamond surfaces are hydrogen-terminated.

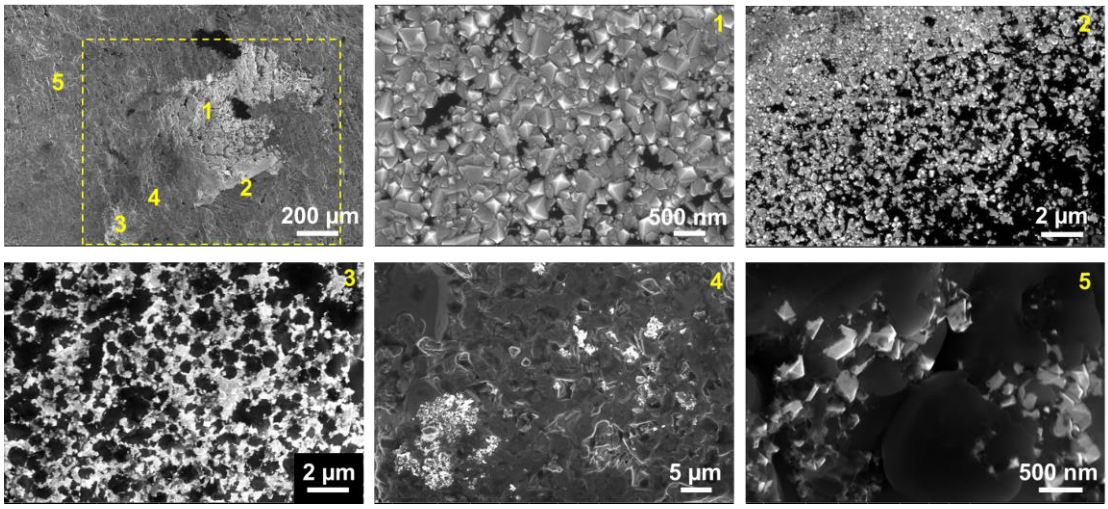

Figure S16. SEM images of the diamonds grown at the center of the bottom surface of the metal alloy piece for a 150 min growth. (a) Large-area SEM image of the bottom part of the solidified liquid metal alloy piece containing as-grown diamonds. For the region marked by a rectangle: (b-f) Magnified SEM images of Regions 1-5 shown in (a).

Region 1 showed that the as-grown diamonds formed a nearly continuous film. Both the density and the size of the as-grown diamonds gradually decreased in the regions away from Region 1. We note most diamonds were found in a submillimeter region in the bottom part of the metal alloy piece, for the 150 min growth runs in which diamond grew (which is almost all of them). Regions farther away from the center, e.g., Region 5, only showed tiny amounts of diamond particles.

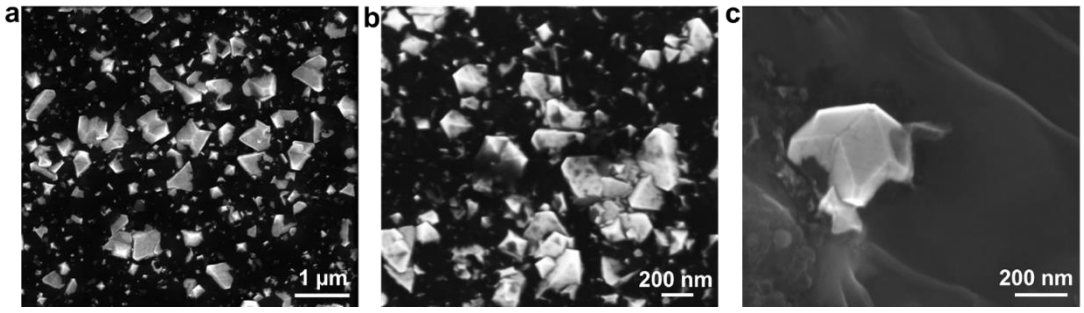

Figure S17. SEM images showing as-grown diamonds 'buried' (partially) in solidified liquid metal after a growth of 30 min.

Fig. S17 show almost all diamond crystals are partially submerged in the solidified liquid metal, and where their exposed apex is/are has much higher brightness (due to diamond being insulating) than the submerged regions (that are surrounded by conductive metal). These SEM images *very strongly* suggest that nucleation and growth occur subsurface.

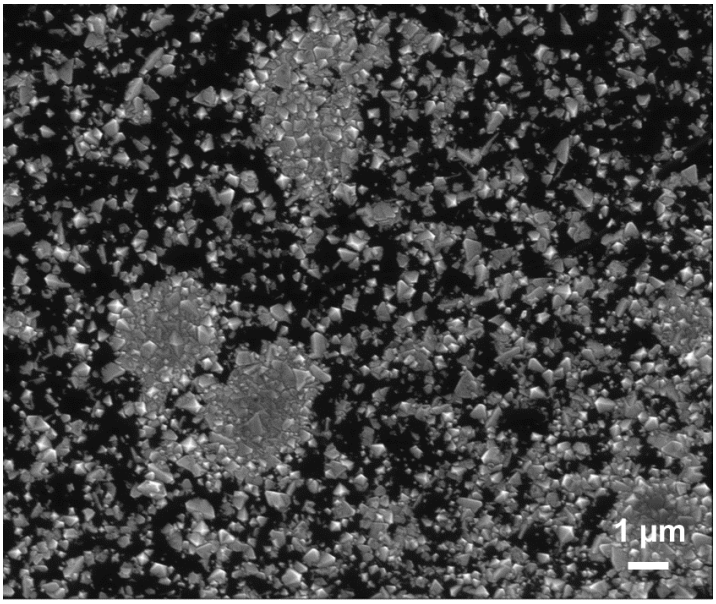

Figure S18. SEM image of the as-grown diamond for a growth time of 60 min.

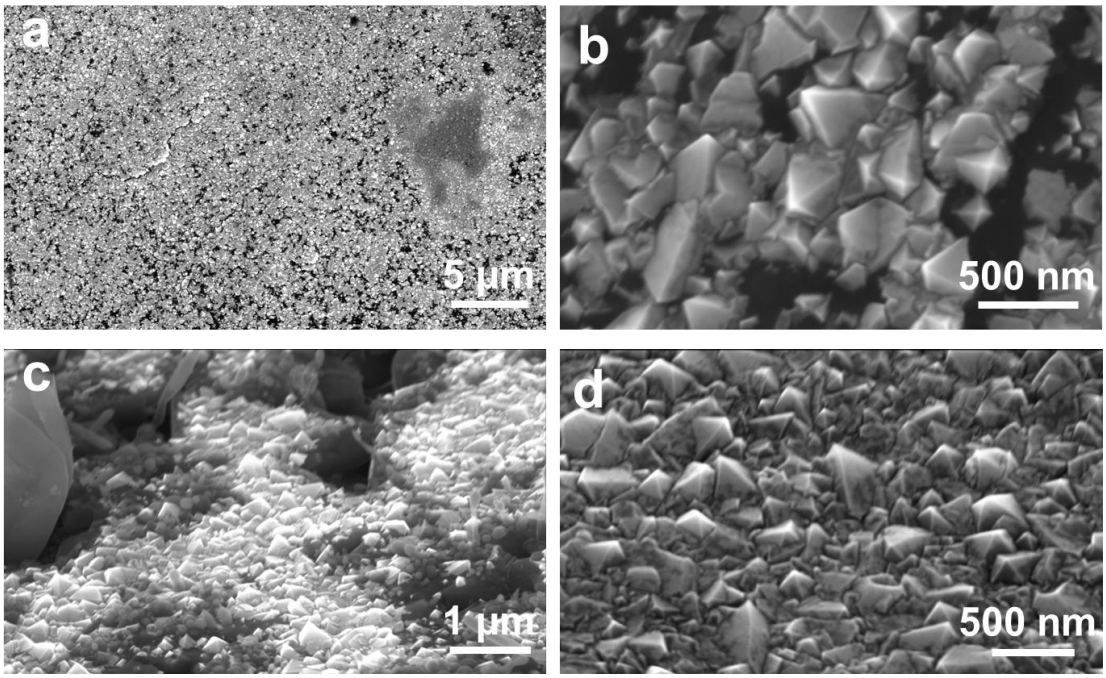

Figure S19. SEM images of the as-grown diamond film for a growth time of 150 min. (a) Low magnification and (b) high resolution SEM images of this diamond film. (c-d) SEM images of different regions of the film acquired at 50.0º tilt of the sample.

Figure S19c-d show regions of the as-grown diamond film with and without gaps. (Gaps are the regions that don't have diamond particles or don't have many diamond particles.)

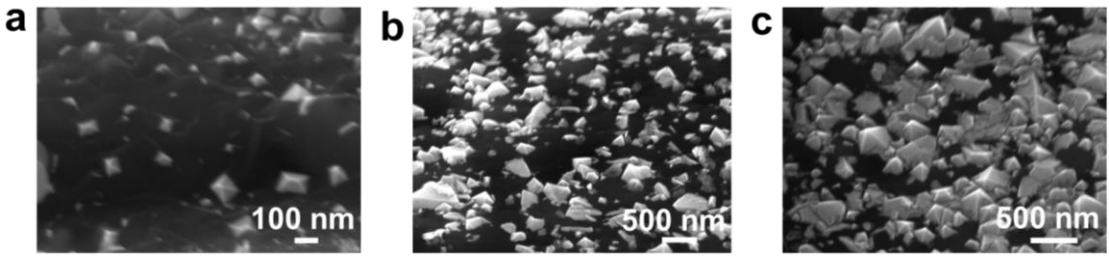

Figure S20. Tilted SEM images (tilt angle 50°) of the as-grown diamond regions for 3 different growth times at 1200 ºC: (a) 15 min. (b) 30 min. (c) 60 min.

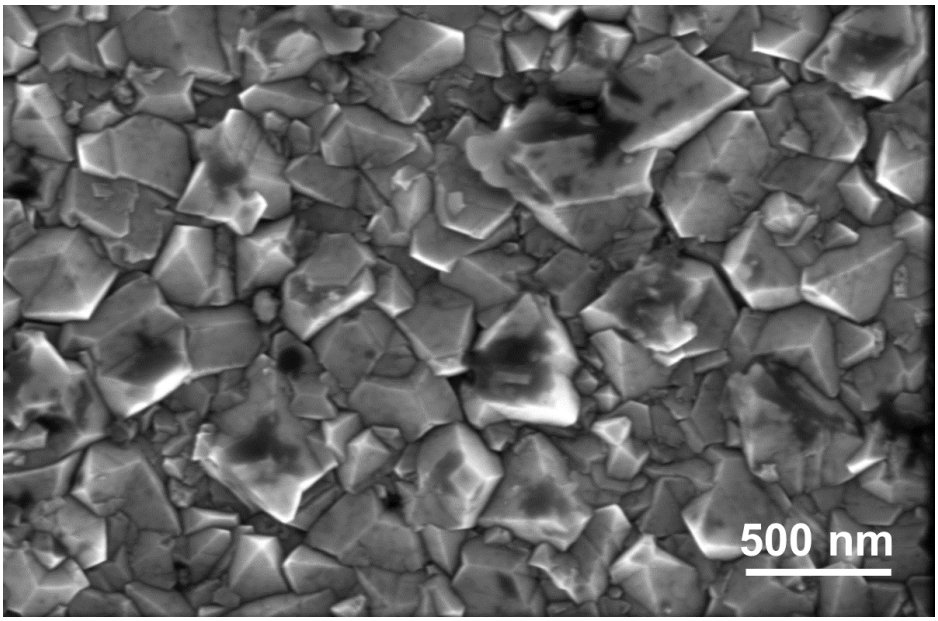

Figure S21. SEM image of a diamond film after growth for 300 min.

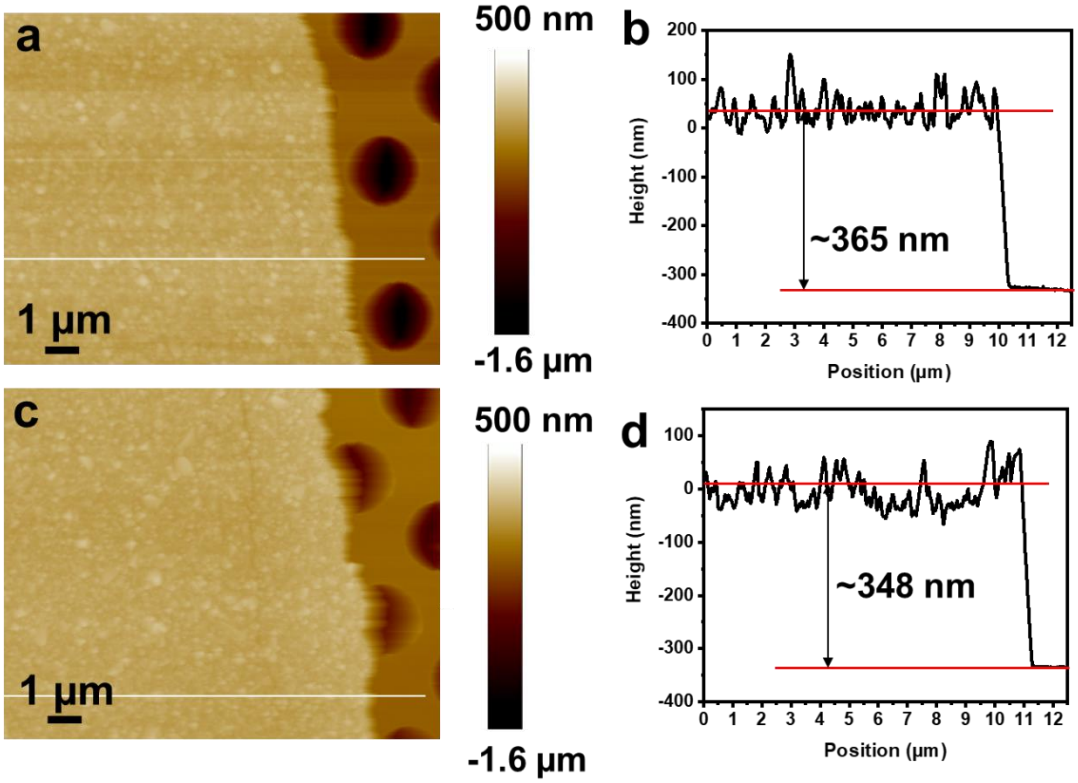

Figure S22. AFM measurements of the thickness of diamond films that were transferred to Quantifoil holey carbon film coated Cu TEM grids. (a) AFM topographic image and (b) correlated height profile of the as-transferred diamond film from a 150 min growth. (c) AFM topographic image and (d) correlated height profile of the as-transferred diamond film from a growth of 300 min.

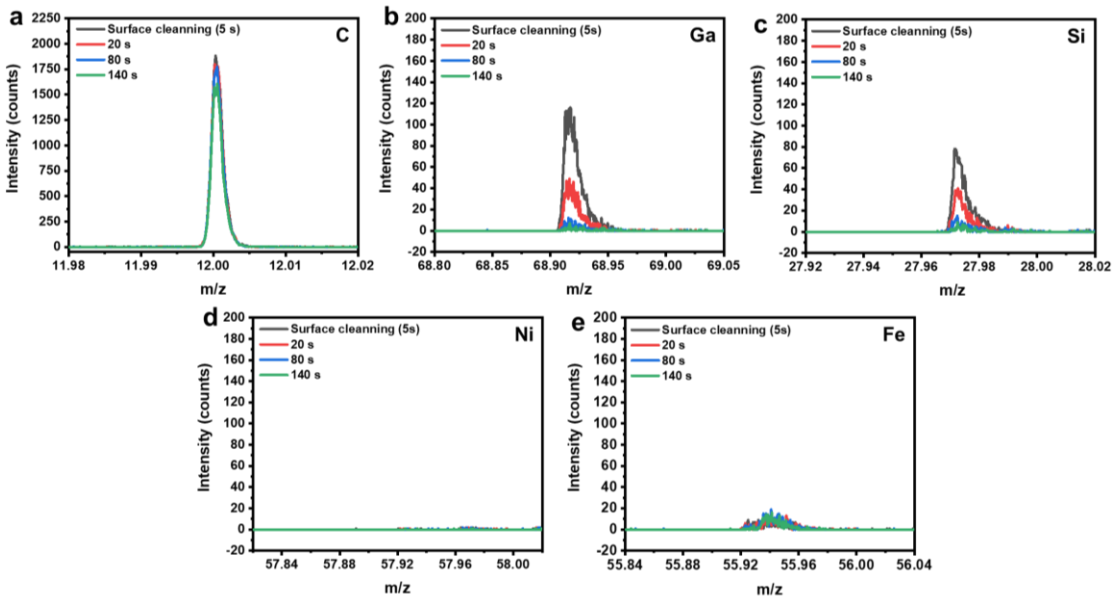

Figure S23. ToF-SIMS spectra of the back side of the as-transferred diamond film (a) C. (b) Ga. (c) Si. (d) Ni. (e) Fe.

The as-grown diamond film on the solidified liquid metal was delaminated by dissolving the metal alloy piece using HCl(aq) solution and then transferred onto a Cu TEM grid with the back side (the side that is interfacing liquid metal during growth) facing up. ToF-SIMS spectra of C, Ga, Si, Ni and Fe were obtained with different sputtering times (to reach a certain depth) to study any contaminants on the *back side* of the as-transferred diamond film. After surface cleaning (5s sputtering), the ToF-SIMS spectra were acquired, with a large intensity of C and weak intensity of Ga and Si observed (Fig. S23a-c). Very weak intensity of Fe that is very likely due to noise, and no signal for Ni (Fig. S23d-e) were found. The intensity of C was constant after 20s (depth of 2 nm), 80s (depth of 8 nm) and until 140s (depth of 14 nm), while the intensities of Ga and Si were dramatically decreased, suggesting that there are only small amounts of Ga and Si contaminants on the as-transferred diamond film back side surface, but none are detectable in the diamond bulk.

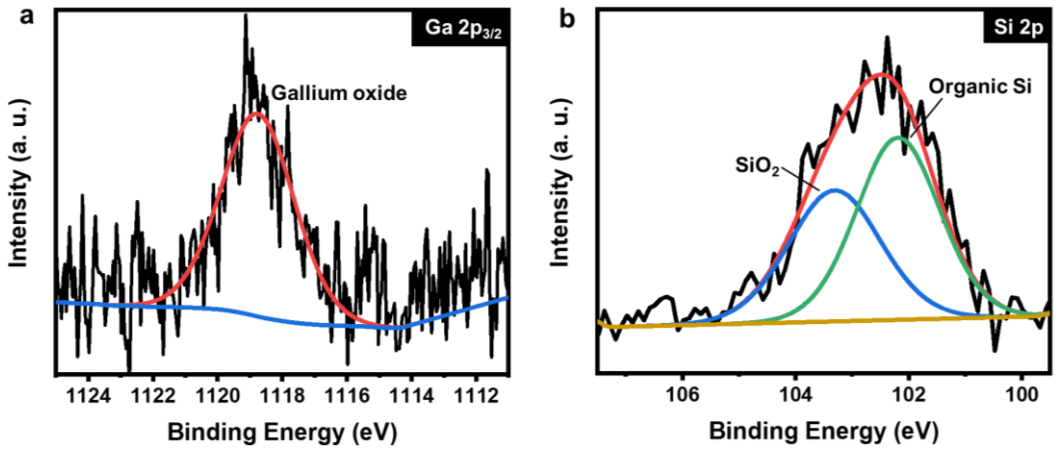

Figure S24. XPS spectra of (a) Ga $2p_{3/2}$ and (b) Si 2p for the back side of as-transferred diamond film.

To further study the chemical states of Ga and Si, XPS analysis (Ga $2p_{3/2}$ and Si 2p) was done (Fig. S24) on this back side surface, and it showed native oxide, 'organic silicon', and Si-O bonding. We did not observe any signal of Ga-C, suggesting that the native oxide of gallium is likely physically adsorbed on the back side surface of the diamond film. The presence of Si-C bonds is of interest as we find that a small amount of Si is critical for our diamond growths (Fig. S5), while SiO_2 is likely formed due to some Si present atop the (backside) of the diamond film.

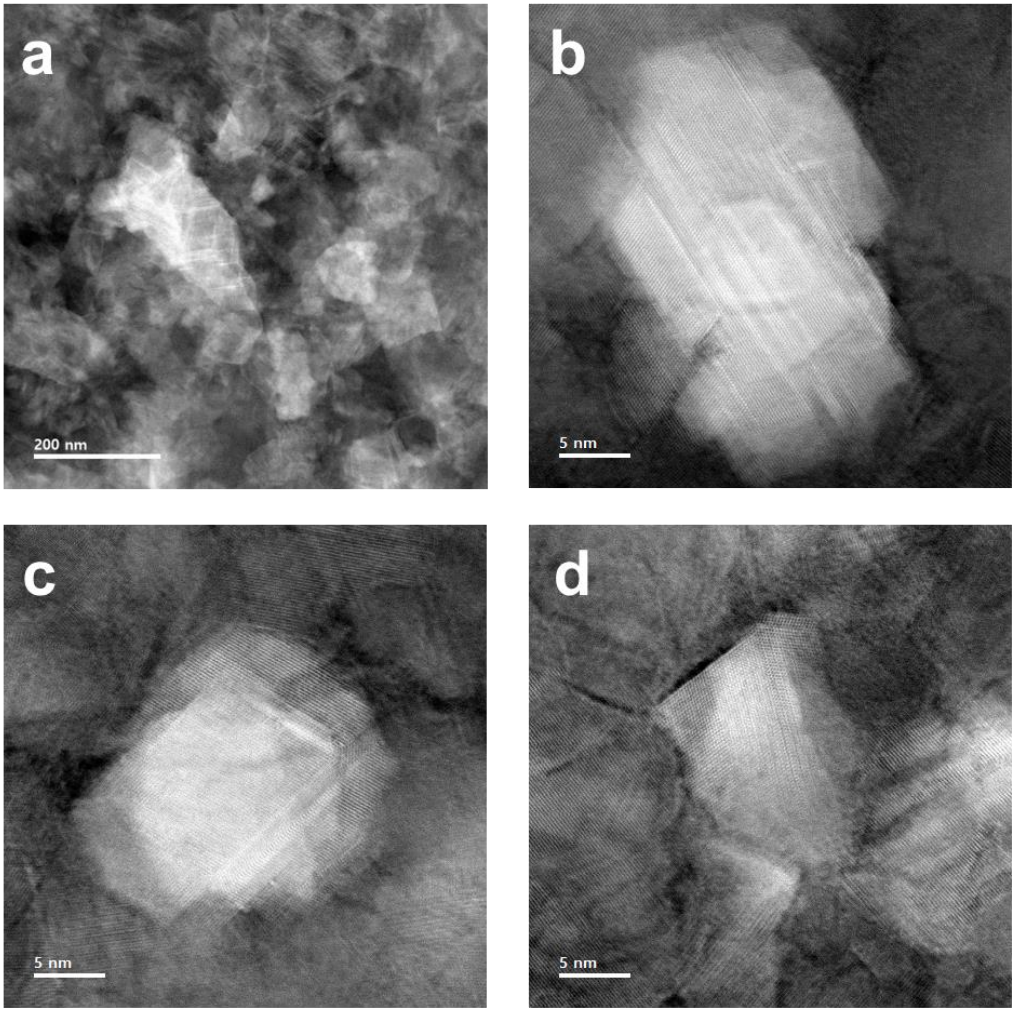

Figure S25. Plan-view TEM images of a diamond film from a growth of 150 min as-transferred on a Quantifoil holey carbon film coated Cu TEM grids. (a) Low magnification TEM image showing the diamond film is composed of diamond crystals of various sizes. (b-d) HR-TEM images of some regions of the diamond film. Note that there are gaps between some diamond crystals.

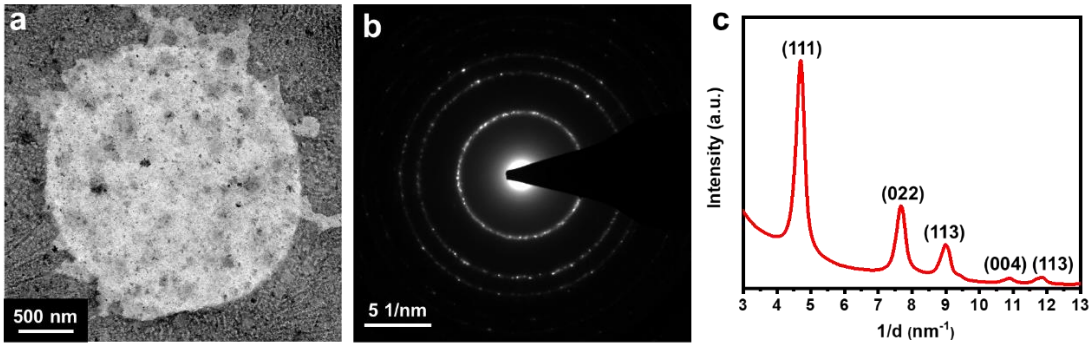

Figure S26. (a) Plan view TEM image of a diamond film (150 min growth) after transfer onto Cu TEM grid coated with a Quantifoil holey carbon film. (b) Selected area electron diffraction (SAED) ring pattern of (a) acquired in the region spanning the hole. (c) The associated radial intensity profile of (b).

The SAED ring pattern and the associated (calculated) radial intensity profile were obtained and show various diamond orientations. There was no graphite found between diamond particles.

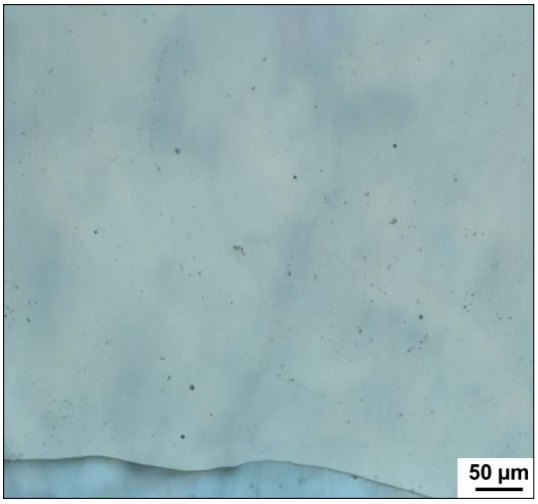

Figure S27. Optical image of an as-transferred diamond film on a 300 nm SiO_2/Si wafer.

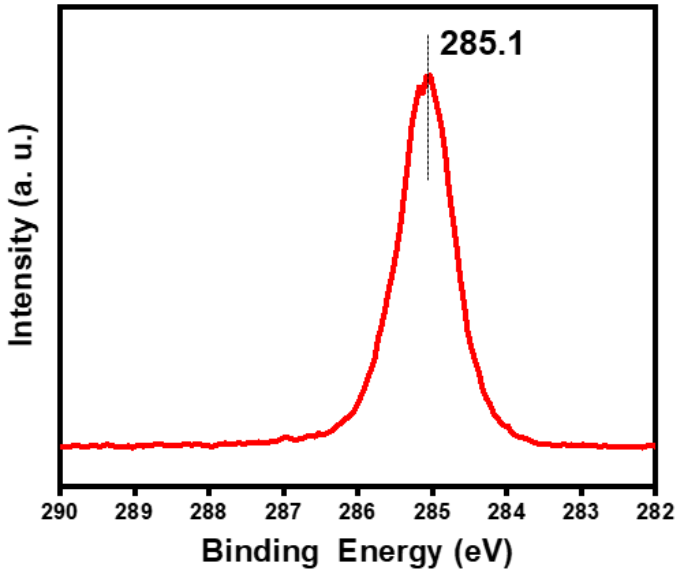

Figure S28. C1s XPS spectrum measured from a transferred diamond film on a 300 nm SiO_2/Si wafer.

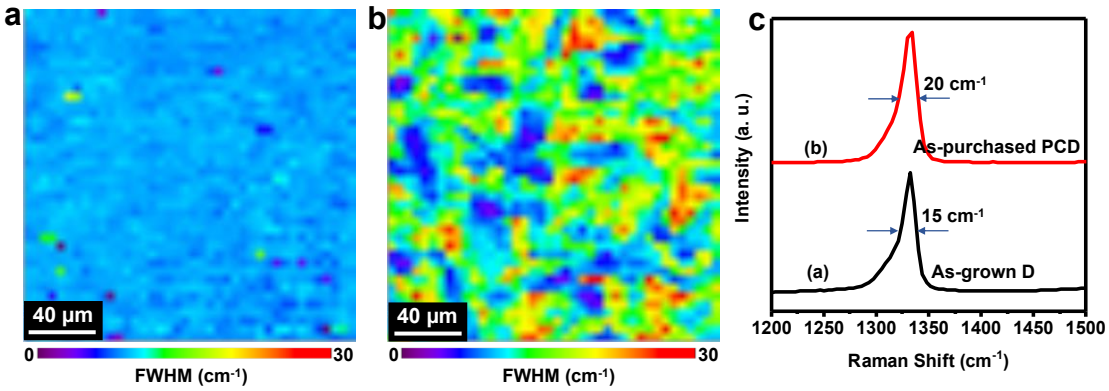

Figure S29. Raman analysis (obtained with 266 nm laser) of as-grown diamond film after transferring onto a 300 nm SiO_2/Si wafer surface and of as-purchased polycrystalline diamond piece. Raman map of FWHM of diamond peak at 1332 cm^{-1} of (a) the as-grown diamond film and (b) the as-purchased diamond substrate. (c) Averaged Raman spectra obtained from the entire mapped regions of (a) and (b).

We did UV Raman mapping of the full width half maximum (FWHM) of the diamond Raman band (at 1332 cm^{-1}) of our as-grown diamond film and an as-purchased polycrystalline CVD-grown diamond piece (5 mm x 5 mm x 0.5 mm, Changsha 3 better Ultra-hard Materials) as shown in Fig. S29. We found that over the 200 μm x 200 μm regions our as-grown diamond film has a more uniform *and* narrower FWHM than the as-purchased one, which shows our as-grown diamond film has higher crystallinity.

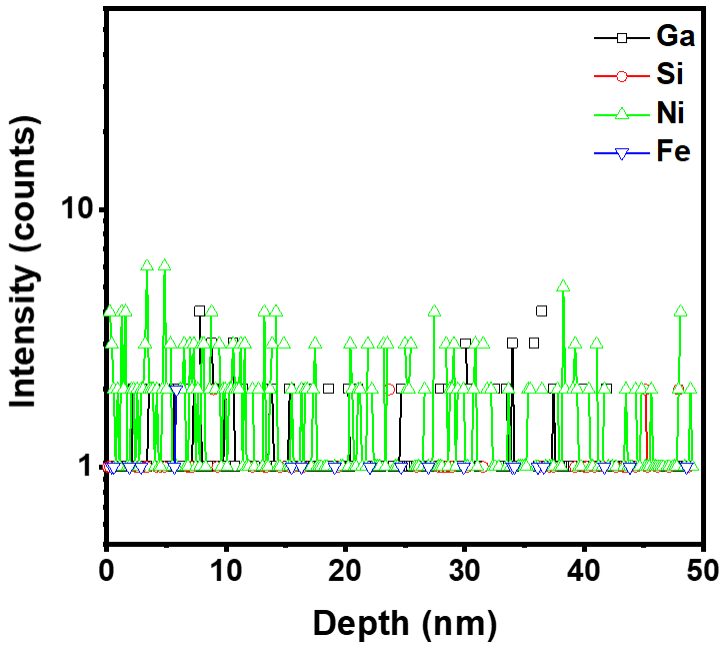

Figure S30. ToF-SIMS depth-profiling (Intensity as function of the depth) obtained on as-grown diamond film.

ToF-SIMS depth-profiling over a lateral size of 100 µm x 100 µm of our as-grown diamond film showed no Ga, Ni, Fe and Si detected in the diamond bulk to 50 nm depth.

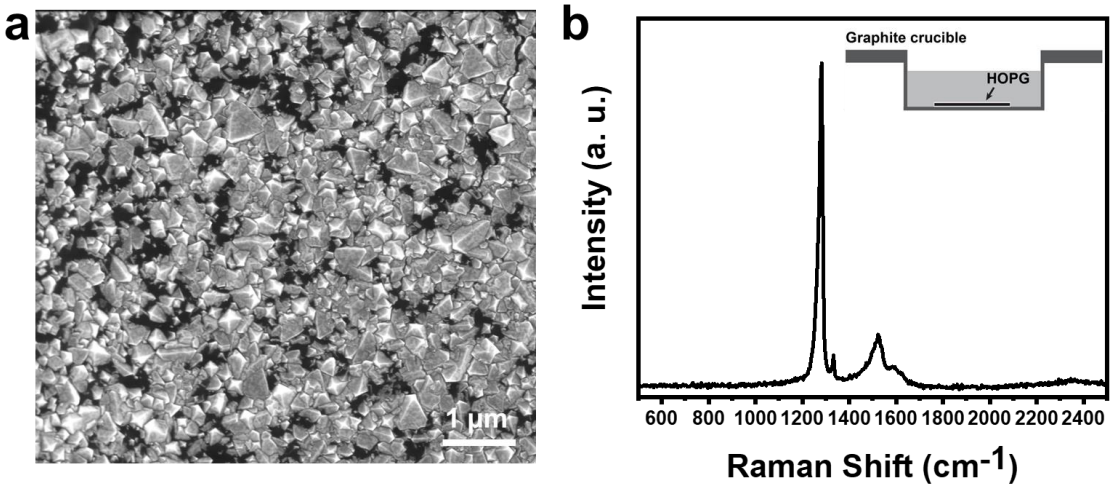

Figure S31. The growth result with $^{13}CH_4$ for 150 min at 1175 °C by inserting one piece of HOPG (about 6 mm x 6 mm x 30 µm) on the bottom surface of the crucible cavity (referred to as ^{13}C-D150-HOPG). (a) SEM image and **(b)** Raman spectrum of ^{13}C-D150-HOPG. Inset in (b): Scheme showing configuration used for the growth.

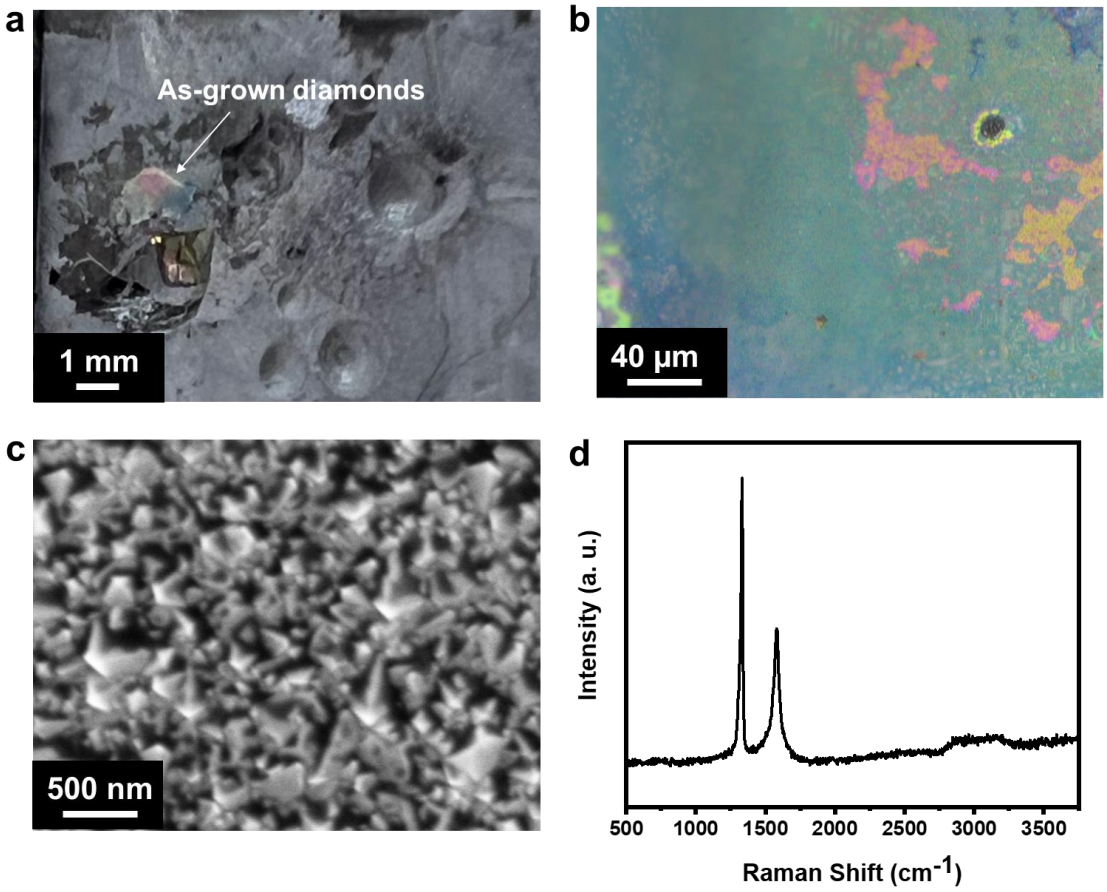

Figure S32. A growth run with a PBN (pyrolytic boron nitride) plate placed at the bottom of graphite crucible (thus between the liquid metal and graphite crucible). (a) Photograph shows the as-grown diamond region. Optical microscope image (b), SEM image (c) and UV Raman spectrum (d) of the as-grown diamond in (a).

We tried placing a pyrolytic boron nitride (PBN) plate (5 mm x 5 mm x 1mm, MTI Korea) at the bottom of the graphite crucible between the liquid metal and graphite crucible. The PBN surface was not etched during our growth (it looks equally smooth as prior to the run). A diamond film of rainbow color was found on the solidified liquid metal surface (Fig. S32). SEM-EDS showed no B or N in the diamond.

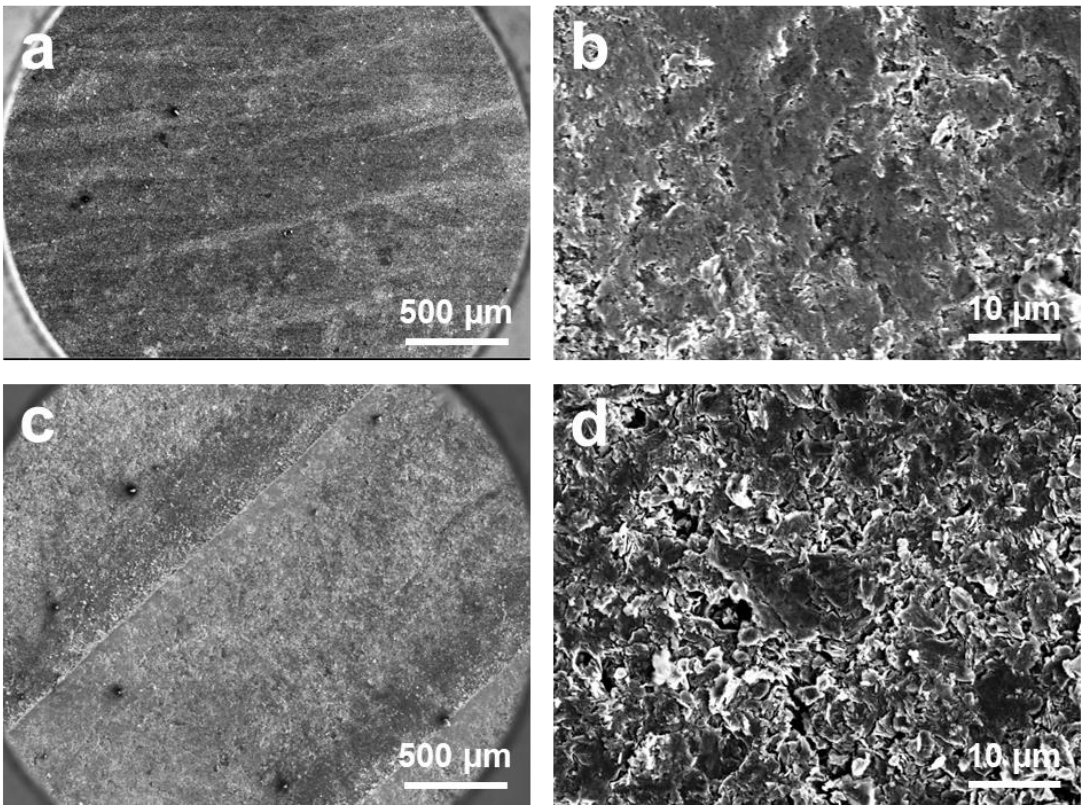

Figure S33. (a-b) SEM images of the bottom surface of the EDM-3 Poco Graphite sheet (the side that interfaces to the liquid metal in our growth runs). (c-d) SEM images of the surface of the graphite crucible.

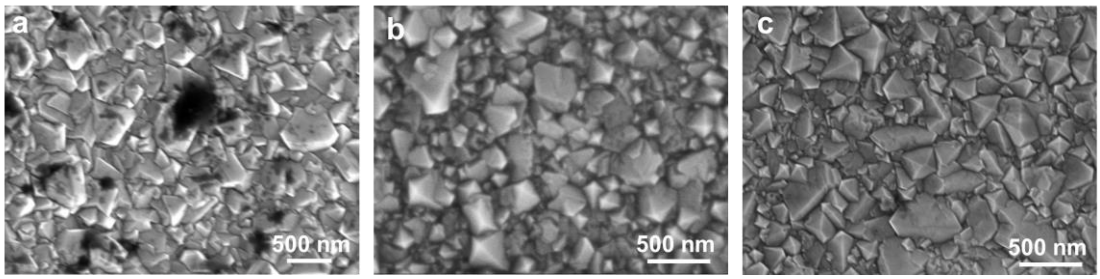

Figure S34. SEM images of (a) ^{13}C- D150-GC, (b) ^{13}C-150D-EDM, and (c) ^{13}C-D150-SEDM.

The size, areal density, and shape of the diamonds in ^{13}C-D150-HOPG (Fig. S31) were essentially identical to ^{13}C-D150-GC and ^{13}C-D150-EDM (Fig. S34). The Raman spectrum of ^{13}C-D150-HOPG (Fig. S31) showed four distinct peaks: diamond peaks of ^{13}D (1283 cm^{-1}) and ^{12}D (1332 cm^{-1}), and the G bands of ^{13}G (1521 cm^{-1}) and ^{12}G (1580 cm^{-1}). The intensity ratio of the ^{12}D to the ^{13}D peak of ^{13}C-D150-HOPG (Fig. S31) is very similar to that of ^{13}C-D150-EDM (Fig. 2b, main text).

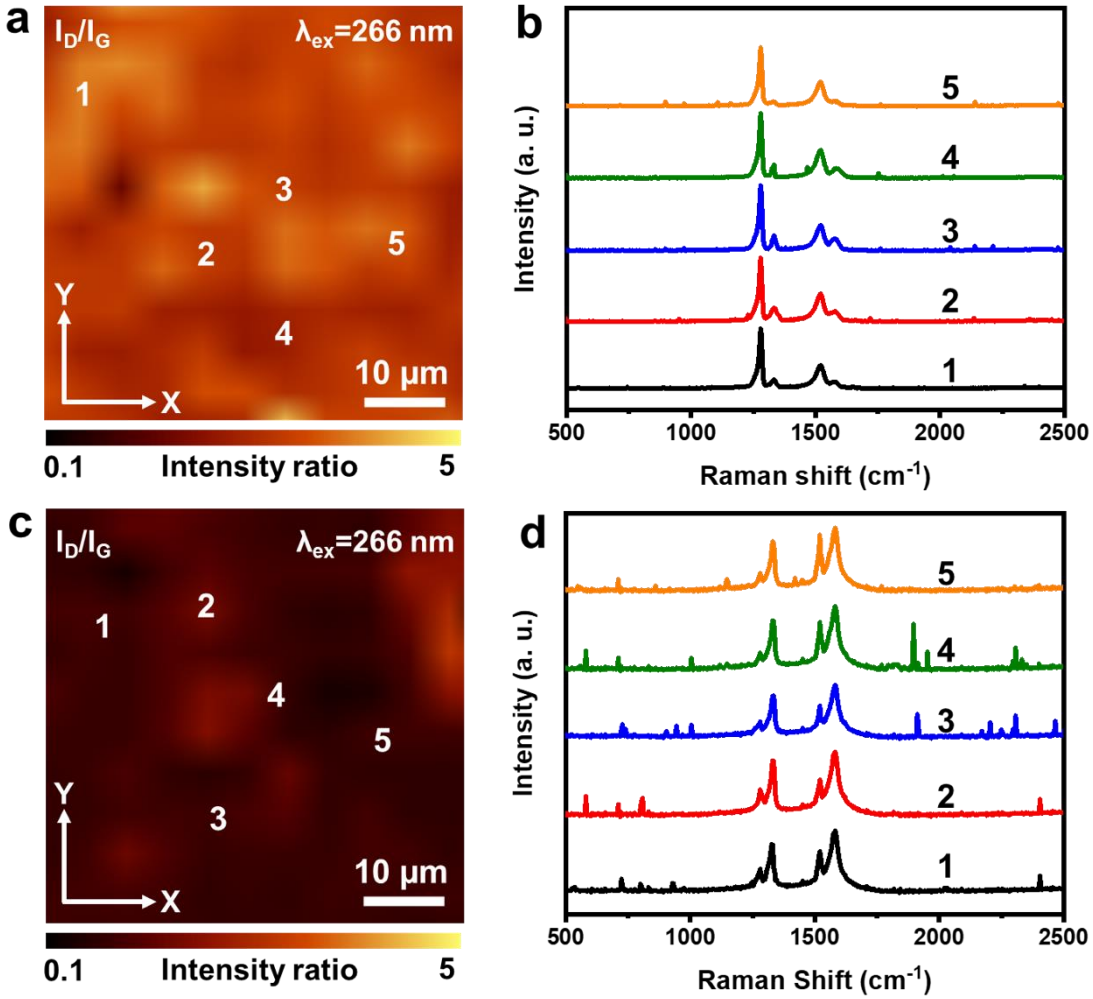

Figure S35. UV Raman analysis of the ^{13}C-D150-EDM and ^{13}C-D150-GC. (a) The Raman map of I_D/I_G ratio of the region in ^{13}C-D150-EDM. (b) Raman spectra taken from the regions marked in (a). (c) The Raman map of I_D/I_G ratio of the region in ^{13}C-D150-GC. (d) Raman spectra taken from the regions marked in (c).

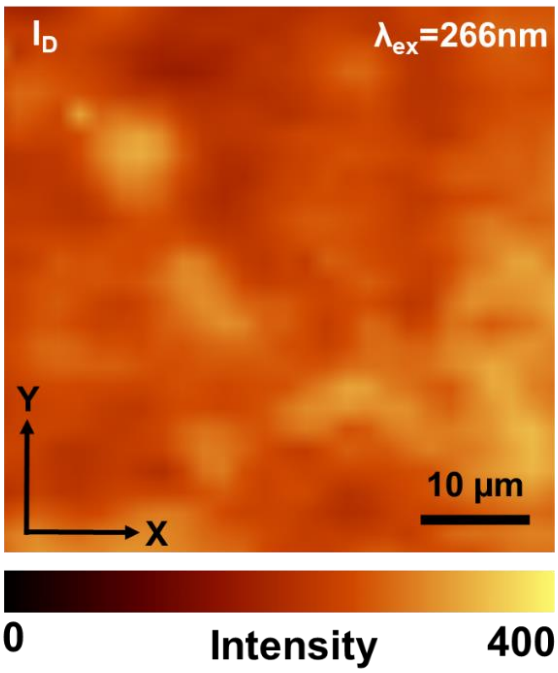

Figure S36. Raman map of ^{13}D intensity of the same region as Fig. 2c for sample ^{13}C-D150-EDM.

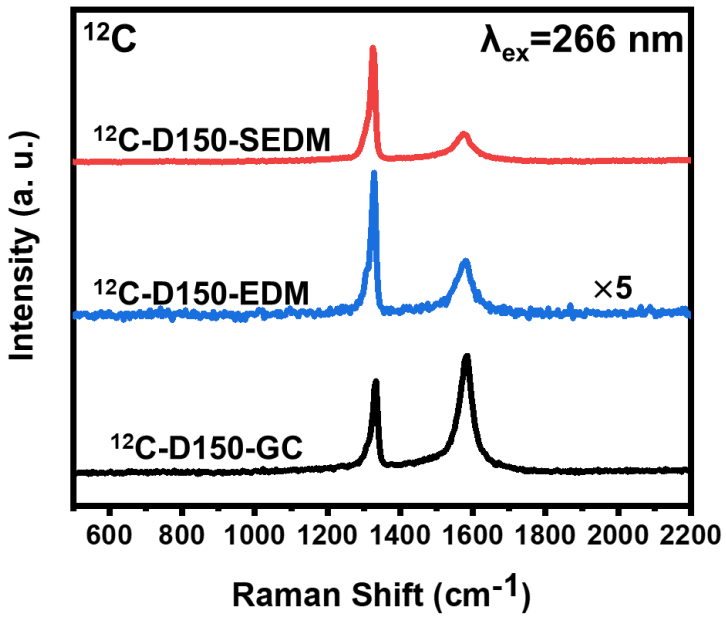

Figure S37. Raman spectra of the as-grown diamonds obtained with normal methane.

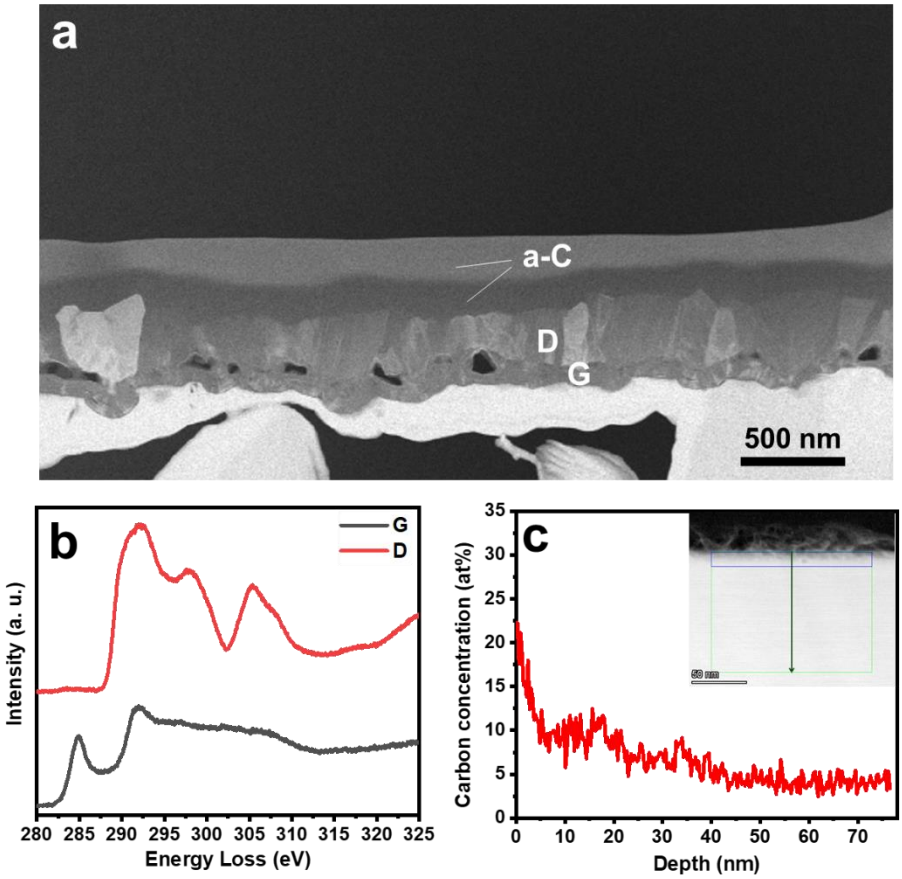

Figure S38. (a) TEM image of the as-grown diamond (D) film and the graphite (G) film beneath the diamond film. (b) EELS spectra obtained from the D and the G regions, respectively. (c) TEM-EDS line profiling showing the carbon concentration of the metal region beneath the G film. M1 and M2 regions were observed, and the M1 region was found to be carbon rich. Inset: High-angle annular dark-field scanning transmission electron microscopy (HAADF STEM) image showing the interface between M1 and M2 regions and showing the position of the TEM-EDS line profiling.

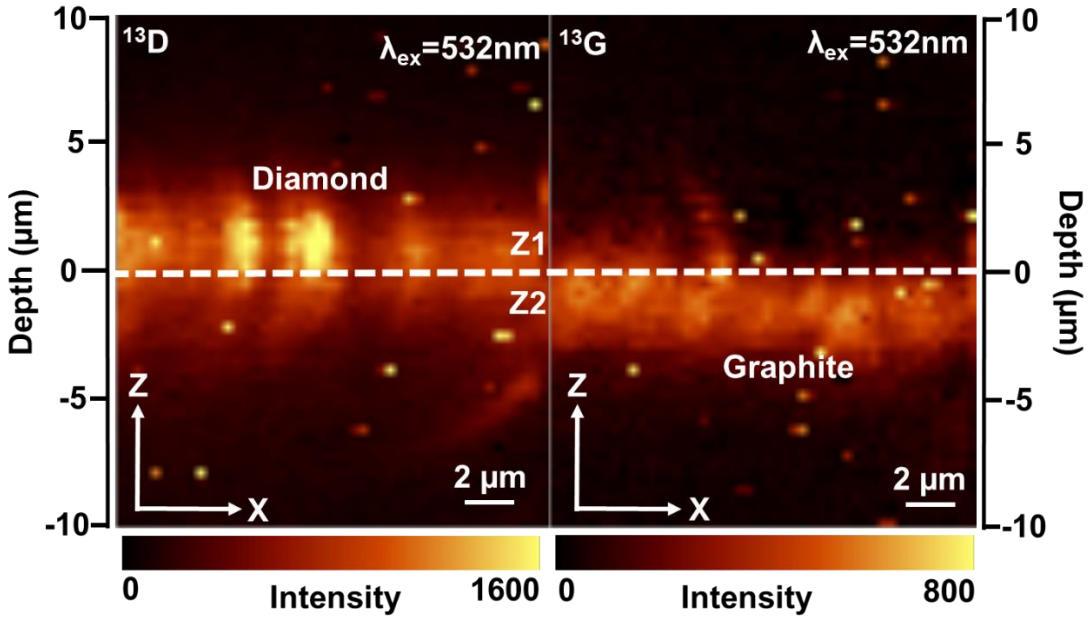

Figure S39. **Raman depth profiling for the regions like those shown in S36. (The same sample, but not the identical region.)**

Raman depth profiling mapping was done to try to further understand the deposited ("grown") carbon. (A focal plane is established, and the sample is then moving 10 microns above this plane, and scanned downwards through 20 microns, see Fig. S39.) We found that the signal of ^{13}D gradually disappeared when the sample was moved from region Z1 to region Z2, and conversely the Raman signal of ^{13}G appeared in the region of Z1 to Z2 where ^{13}D had gradually disappeared. This suggests that graphite was primarily formed underneath the continuous diamond film. We note that a *tiny* graphite G band signal was detected when the focal plane was located within the diamond film region, possibly due to the discontinuity of the as-grown diamond film or that a very small amount of graphite was grown along with diamond.

That graphite was formed primarily underneath diamond is also suggested by: i) cross-section TEM images showing the graphite structures were underneath diamond crystals with a clear interface (Fig. S38a); ii) EELS spectra acquired from 20 randomly selected regions over the as-grown diamond regions showing only diamond phase with the absence of graphite phase (Fig. 3e); iii) plan-view TEM images together with SAED patterns of the transferred diamond film showing only diamond phase with the absence of graphite phase (Fig. S25-26); iv) C1s XPS spectrum of an as-transferred continuous

diamond film showing only sp^3-bonded carbon without sp^2-bonded carbon (Fig. S28). For those cases where graphite was found underneath diamond, it suggests that diamonds grow first in the C-rich subsurface region of the liquid metal, followed by the growth of graphite. And we note that graphite was not always formed underneath the as-grown diamonds; for example, there are regions where the as-grown diamonds directly contact the solidified liquid metal surface (Fig. 3a).

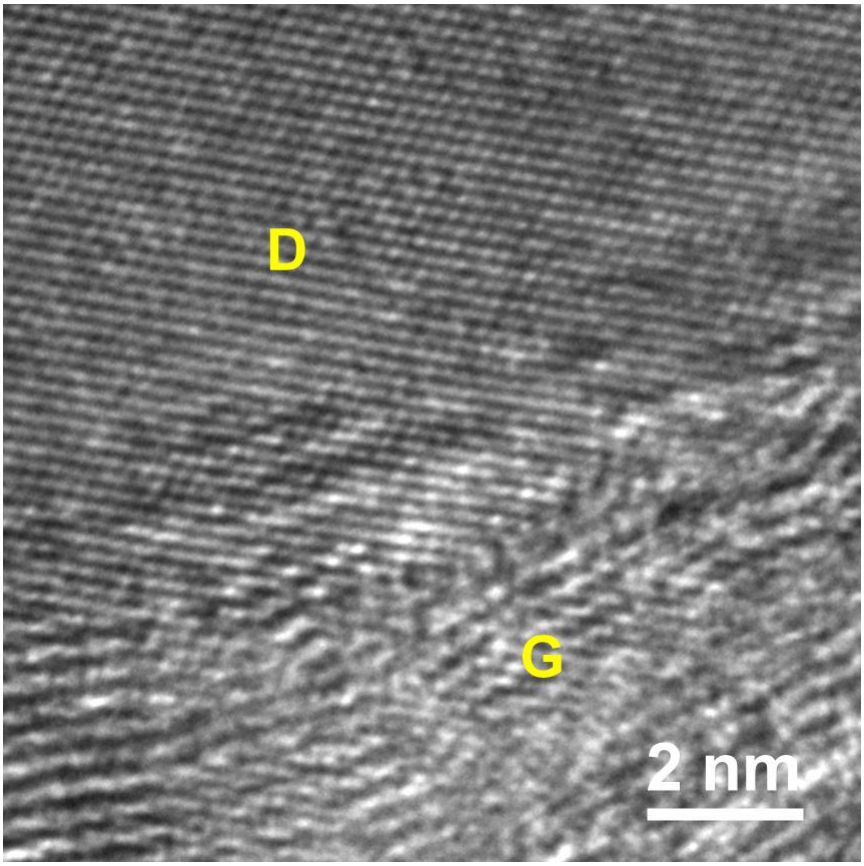

Figure S40. HR-TEM image obtained from the region in Fig. S38a showing the interface between as-grown diamond and as-grown graphitic carbon.

Our cross-section TEM image (Fig. S40) suggest that while there is a clean interface between the as-grown diamond film and the as-grown graphite, high-resolution imaging at such interfaces shows no evidence of any epitaxy between diamond and graphite lattices and the absence of bonding between diamond and graphite at the interface regions, suggesting that diamond-to-graphite or graphite-to-diamond transformation is not likely have occurred under our growth conditions[3-5].

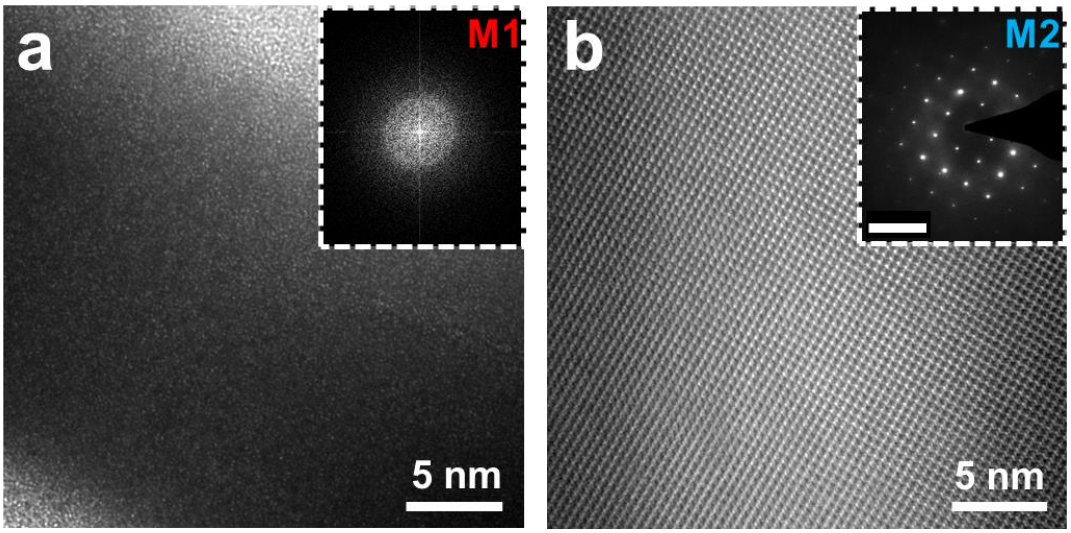

Figure S41. (a) HR-TEM image of the M1 region of D30 (inset: FFT pattern). It shows that the M1 region of D30 is amorphous. (b) HR-TEM image of the M2 region of D30 (inset: SAED pattern, the scale bar is 5 nm^{-1}). It shows that the M2 region of D30 is crystalline.

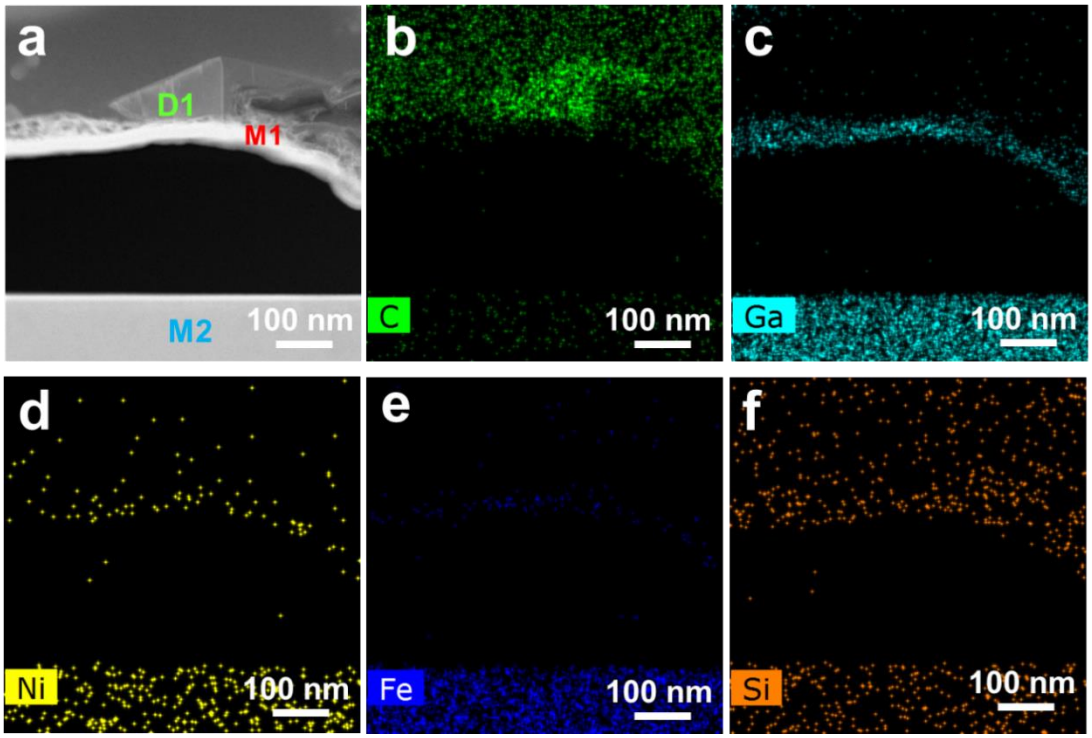

Figure S42. (a) Cross section TEM image showing the region contained D1 and the metal beneath D1 (this image was also used in Fig. 3h). (b-f) The corresponding EDS elemental mapping showing these elements: (b) C, (c) Ga, (d) Ni, (e) Fe, and (f) Si.

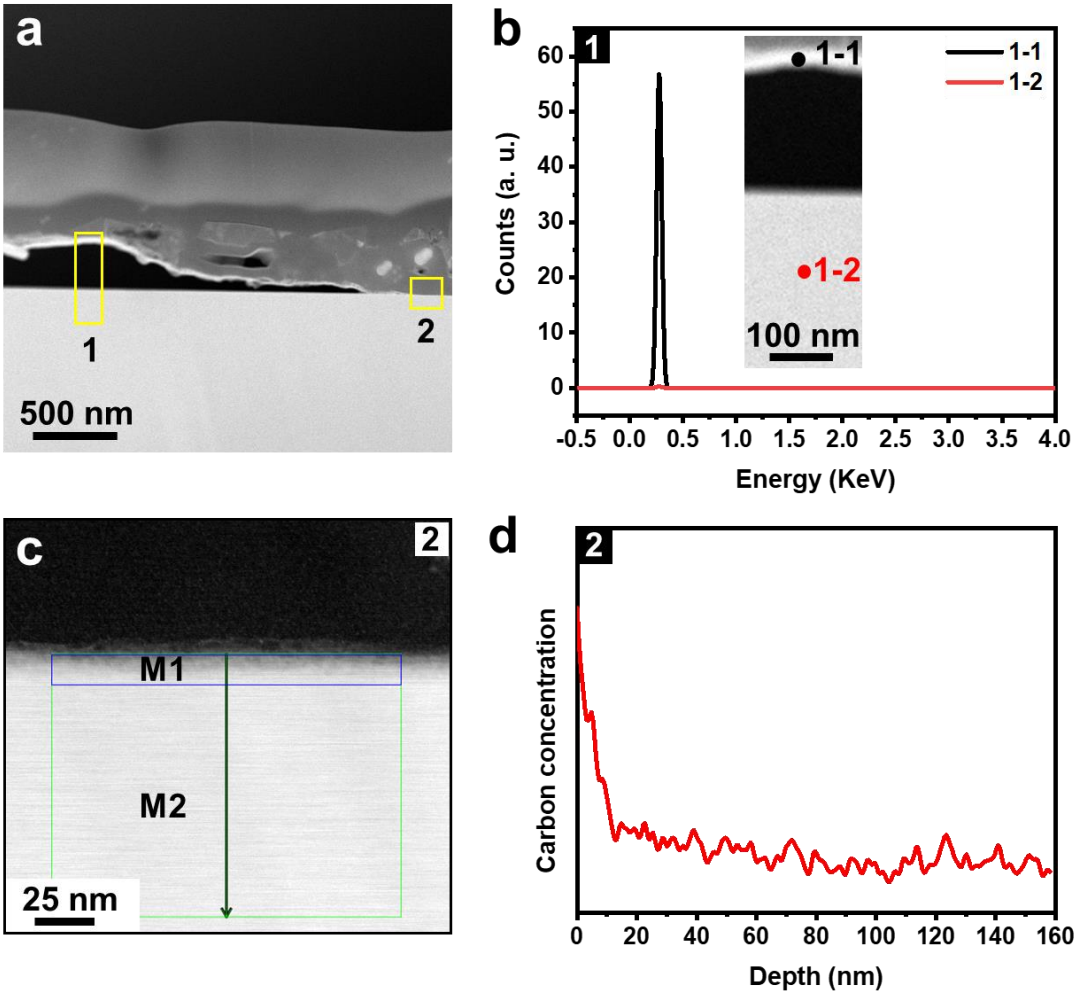

Figure S43. TEM-EDS analysis of carbon concentration in M1 and M2 of sample D30. (a) Cross-section TEM image of D30 (this image was also used in Fig. 3g). (b) Two EDS spectra of carbon were obtained from the delaminated M1 region and the crystalline M2 region (Inset: HAADF STEM image correlated to region 1 marked in (a)). The peaks at the position of ~0.25 KeV in the spectra are coming from carbon. (c) HAADF STEM image correlated to region 2 marked in (a). (d) TEM-EDS line profiling along the line marked in (c) showing the atomic concentrations of carbon in M1 and M2 regions.

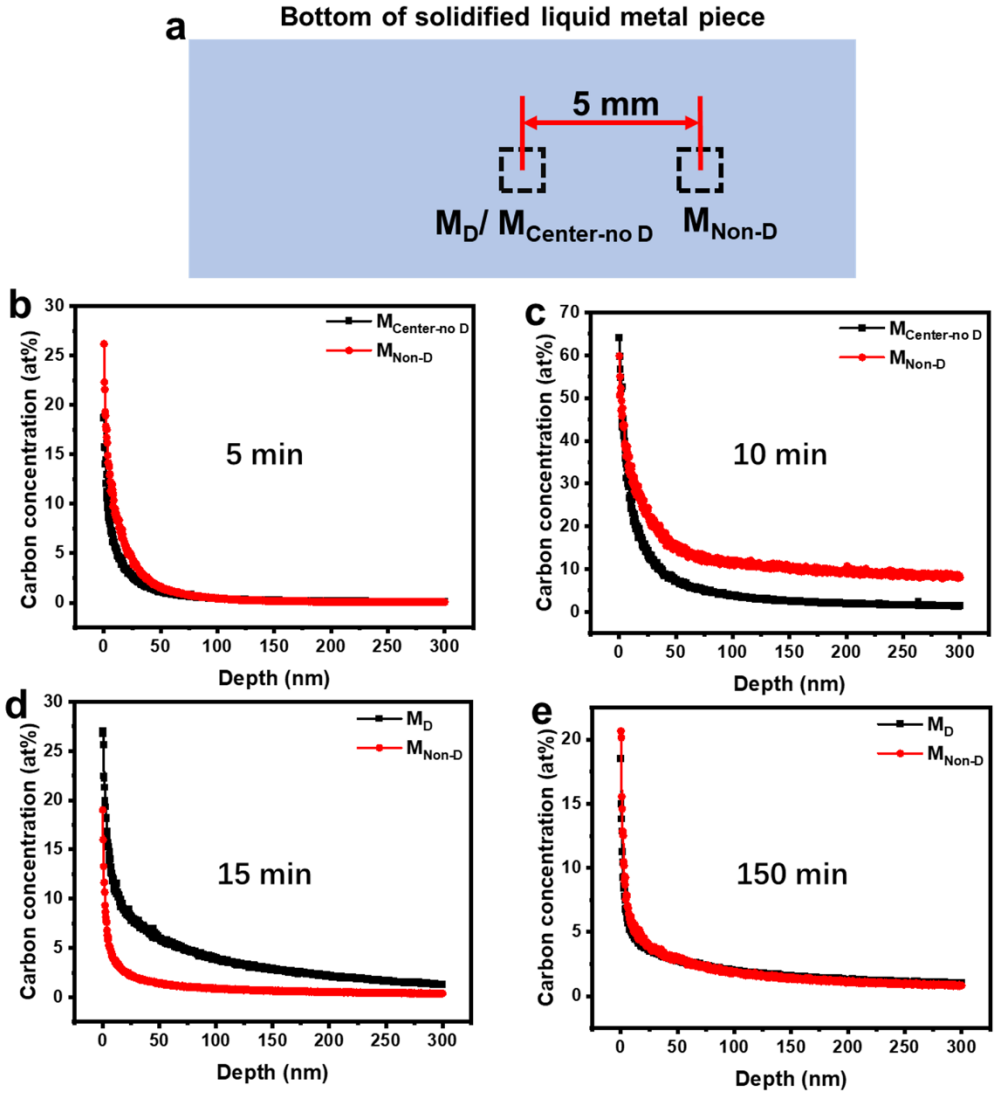

Figure S44. ToF-SIMS depth-profiling of carbon ($^{13}C^-$) concentrations obtained on two different regions of the solidified liquid metal pieces. (a) A scheme showing the two regions of solidified liquid metal piece that we investigated. (b-e) ToF-SIMS depth-profiling of the two regions on solidified liquid metal pieces after growth for (b) 5 min, (c) 10 min, (d) 15 min, and (e) 150 min.

We did 4 'growth runs' with $^{13}CH_4$ and H_2 for, respectively, 5 min, 10 min, 15 min, and 150 min.

We delaminated (by using a double-side copper tape) the entire bottom surface of the solidified liquid metal for the 150 min run, thereby 'uncovering' the metal region that was underneath the as-grown diamond film ("M_D"), and another metal region ~ 5 mm away that did not have diamond grown on its surface ("$M_{Non\text{-}D}$"; please see Fig. S44a), but where there was some graphite. We note that we did not find diamonds grown for the 5 min and 10 min exposures to $^{13}CH_4$ and H_2. For these two cases, "$M_{center\text{-}no\ D}$"

refers to the center region but with no diamonds present (this center region is where diamonds are typically found on the solidified liquid metal piece for longer growth times such as our standard 150 min, but also 15 min, 30 min, etc). We then used ToF-SIMS depth-profiling to study the concentration of carbon for the $M_{center\text{-}no\ D}$ and $M_{Non\text{-}D}$ regions for the 5 and 10 minute 'growth' runs, and the M_D and $M_{Non\text{-}D}$ regions for the 15 and 150 min 'growth runs'.

The center regions and "Non-D" regions show ^{13}C for all 4 samples. The concentration of ^{13}C, [^{13}C], was calculated by using a reference sample: A single crystal Ni(111) foil uniformly loaded with 0.77 at% ^{13}C.

Briefly, a "home-made" single crystal Ni(111) foil[6] (100-μm-thick, see, e.g.) was exposed at a high temperature in a Joule heating system (that also allows for extremely rapid cooling of the foil piece) to $^{13}CH_4$ gas to "dissolve" ^{13}C into the Ni(111) foil, and from the weight change of the foil before and after feeding with ^{13}C, a Ni(111) foil containing 0.77 at% ^{13}C was obtained with all ^{13}C in its interior and essentially none on the surface of this foil ^{13}C. We then did ToF-SIMS depth-profiling of this foil and found that the $^{13}C^-$ ion signal is 15.3x stronger than the Ni^+ ion (uniformly 15.3, for all isotopes of Ni) signal. We then used this pre-factor of 15.3 to calculate the [^{13}C] from the intensities of ^{13}C and Ni measured on/in our solidified liquid metal pieces, because the solidified liquid metal pieces have the known percentage of 11.00 at% Ni.

For the 5 min run (Fig. S44b), we found ^{13}C present in the metal subsurface and down to a depth of ~100 nm for both regions, and $M_{Non\text{-}D}$ (~26 at% at surface) has slightly higher ^{13}C concentration, [^{13}C], than $M_{center\text{-}no\ D}$ (~18 at% at surface). The [^{13}C] of both regions decreases to close to zero for depths larger than 100 nm.

For the 10 min run (Fig. S44c), the [^{13}C] in the $M_{center\text{-}no\ D}$ is ~65 at% at surface, and $M_{Non\text{-}D}$ is ~60 at% at surface. For the depth of ~10 nm at beginning, the [^{13}C] in $M_{Non\text{-}D}$ is very similar to $M_{center\text{-}no\ D}$. From the depth of ~ 10 nm to the final depth of 300 nm, the [^{13}C] in $M_{Non\text{-}D}$ is higher compared to $M_{center\text{-}no\ D}$.

For the 15 min run (Fig. S44d), the [^{13}C] at the surfaces of M_D and $M_{Non\text{-}D}$ regions are ~27 at% and ~18 at%, respectively.

Thus, at 10 min no diamonds have grown, but diamond had clearly grown by 15 min.

The significantly smaller [^{13}C] found subsurface in the solidified liquid metal regions for the 15 min run compared to the 10 min run, is very likely (it essentially must be) due to the nucleation and growth of diamonds that consumes the ^{13}C (and generally for runs with normal methane: that consumes the subsurface carbon) inside the liquid metal.

The larger [^{13}C] of the M_D region compared to the $M_{non\text{-}D}$ region as a function of depth for the 15 min run suggests why diamonds are found where they are in our growths: We suggest that growth occurs in the central region at the bottom of the liquid metal contacting the EDM-3 sheet due to a lateral gradient in the concentration of dissolved carbon (here, studied with ^{13}C), and that this C concentration gradient inside the liquid metal at its bottom (sub-surface) region is likely created by the temperature gradient (measured with inserted thermocouples as described Fig. S2 in Supplementary Information), and possibly additionally contributed to by geometric factors (the geometry of our crucible). That is, a "flow" of dissolved C is generated towards the region where diamond nucleates, grows, and merges into a polycrystalline film.

And that under our growth conditions, the concentration of subsurface C atoms at about 10 minutes is so high that the supersaturation is *very close* to nucleating diamonds. Nucleation evidently occurs followed by rapid growth of diamond particles between about 10 minutes, and less than 15 minutes.

For the 150 min run (a polycrystalline diamond film formed; see Fig. S44e), the [^{13}C] at the surfaces of M_D and $M_{Non\text{-}D}$ regions are ~18.5 at% and ~20.5 at%, respectively, and the [^{13}C] of M_D and $M_{Non\text{-}D}$ are very similar for all depths to a depth of 300 nm.

Our TEM-EDS results showed that the concentration of C in the solidified liquid metal piece after a 150 min growth (TEM-EDS, Fig. 3d, Fig. S38; of cross sections made with SEM FIB cutting; that is, the "M1" region) was high in the subsurface region to a depth of ~30 nm, with ~26.5 at% at the solidified liquid metal region directly adjacent to the diamond film. This value is close to the value measured by using ToF-SIMS (~18.5 at% at the surface; see Fig. S44e).

The ToF-SIMS depth-profiling shows that the subsurface region contains a relatively large concentration of ^{13}C even to a depth of ~100 nm (Fig. S44b-e) for the 5, 10, 15, and 150 min runs. Note that TEM-EDS has a threshold detection of ~1 at% and ToF-

SIMS a threshold of ppm to ppb, thus the longer "tail" of decreasing [^{13}C] in the ToF-SIMS depth-profiling. What is important is that these two independent experimental methods (ToF-SIMS and TEM-EDS) show a high percentage of C in the near surface and 'sub-surface' regions. *This sub-surface region is where the diamonds nucleate and grow.*

SEM images show almost all diamond crystals are partially submerged in the solidified liquid metal (at the early stages of growth, prior to when they have merged to make a film: such as for growth times of 15 (Fig. 1d) and 30 min (Fig. S17)). These SEM images *very strongly* suggest that nucleation and growth occur subsurface when the [C] reaches a critical level in the growth region (this central region), and C flowing towards the growth region from the surrounding regions 'feeds' further growth.

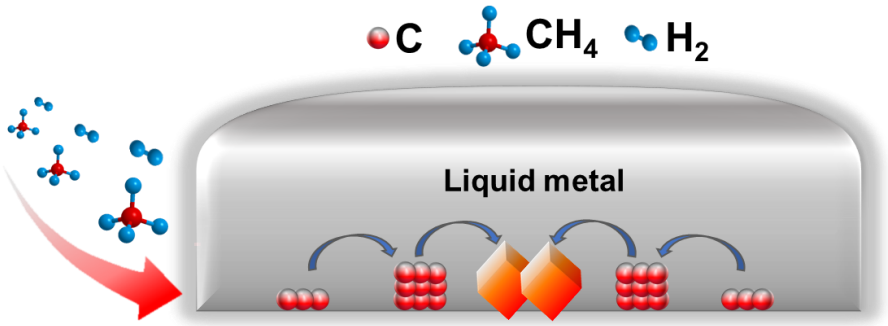

Figure S45. Scheme showing the growth of diamond at the bottom surface of the liquid metal.

With our ToF-SIMS depth-profiling data (Fig. S44) as well as our measurement of the temperature gradient present at the bottom of the liquid metal in conditions essentially identical to our growth runs (Fig. S2, Table S1), we present a highly plausible model for how diamond nucleates and grows (Fig. S45): in the central region when a very high concentration of C atoms is reached, diamond nuclei form (assisted by Si atoms likely at the pre-nuclei stage that stabilize small clusters) that grow and are constantly 'fed' new carbon by the surrounding, higher temperature regions nearby.

Note S1. Activation of methane on liquid metal surfaces.

We have calculated the activation of methane (CH_4) as it might happen at the liquid metal (LM) surface (gas/liquid interface) with C-H bond dissociation yielding CH_3 and H radicals adsorbed at the liquid metal surface.

The radial distribution function (RDF) of the liquid Ga structure was obtained by ab initio molecular dynamics (AIMD) simulation at 375 K and 1300 K as shown in Fig. S46. The highest peak at 375 K (~2.7 Å) decreased at 1300 K, due to the formation of low-coordinated atoms at the surface. Per our computational study the liquid Ga surface structure is disordered at high temperature (1300 K) and small clusters appear and disappear dynamically. In this regard, we note a computational study of the Indium (In) liquid surface at 1200 K that reported small surface clusters playing a critical role for dissociation of the first C-H bond in methane adsorbed on the liquid indium surface[7].

We found that the C-H bond dissociation energy on a solid Ga slab is 0.83 eV (Fig. S47; note that this is a zero Kelvin calculation, thus E (calculated electronic energy) values are shown). Of course, the liquid metal is not crystalline gallium, but we note this low value as interesting.

To probe possible CH_4 activation at the surface of the liquid Ga-Fe-Ni mixture, Ga atom, Ga-Ga (dimer), and Fe and Ni atoms, were considered as individual entities, and (separately), Ga and Ga-Ga were also located on top of a particular mixture of Ga-Fe-Ni as described further below. The overall reaction of interest is:

$$CH_4(g) + \text{cluster} \rightarrow CH_3(ads) + H(ads) \quad (1)$$

And we consider Reactions (2) and (3) that yield Reaction (1):

$$CH_4(g) + \text{cluster} \rightarrow CH_4(ads) \quad (2)$$

$$CH_4(ads) \rightarrow CH_3(ads) + H(ads) \quad (3)$$

in which “ads” means “adsorbed”, and the energy changes are ΔE_1 and ΔE_2 for Reactions (2) and (3), respectively (or ΔH_1 and ΔH_2, or ΔG_1 and ΔG_2, as discussed below).

The adsorption free energies of methane (ΔG_1) on different clusters are shown in

Table S3 and S4, in which G(CH_4(ads)) is the (Gibbs) free energy of the CH_4 adsorbed on the cluster, G(CH_4) the free energy of CH_4 in the gas phase, and G(cluster) is the free energy of the 'cluster" such as (Ga atom, Ga dimer, Fe atom, Ni atom; or these atop of Ga_9FeNi as described below). CH_4 can be adsorbed on an Fe atom in the quintet spin state at -0.60 eV, indicating strong orbital hybridization. For other clusters, methane is physiosorbed on the surface with a weak binding energy.

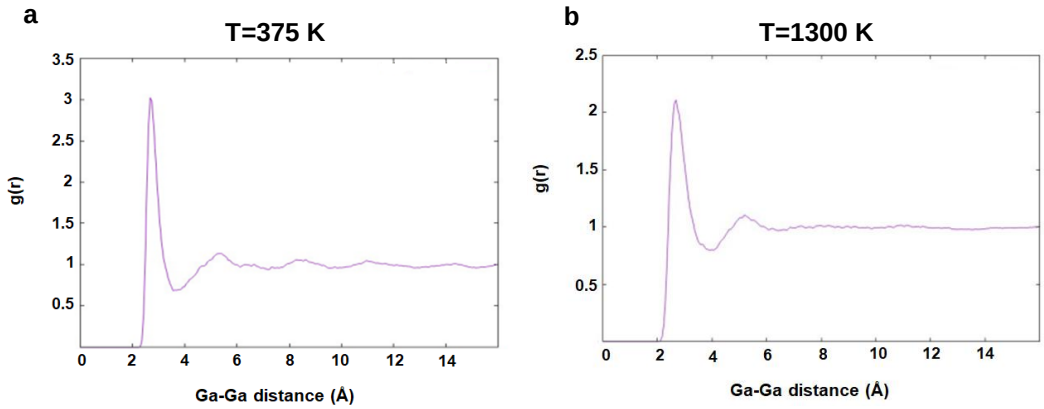

Figure S46. (a-b) Computed radial distribution function (RDF) of liquid Ga at (a) 375 and (b) 1300 K using AIMD trajectories.

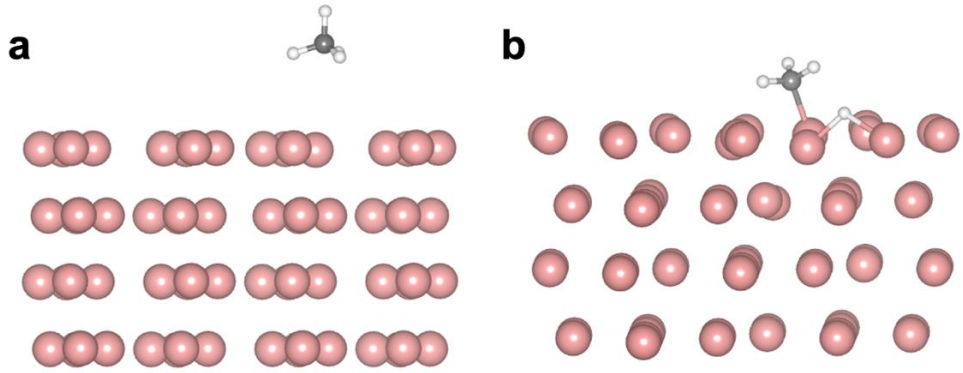

Figure S47. (a-b) Optimized structure of (a) CH_4(ads) and (b) CH_3(ads) + H(ads) on Ga slab surface (100), where ΔE_1 is -0.17 eV and ΔE_2 is 1 eV. All layers in the Ga slab were fully relaxed with VASP at 0 Kelvin.

So that we are comparing "apples to apples" and not "apples to oranges" we briefly discuss the meaning of ΔH and ΔG to correctly account for the dramatic impact of adsorption on changing ΔH, compared to the gas phase reaction. The gas phase reaction ΔH and ΔG values are shown below (Fig. S48).

Reaction Equation: $CH_4(g) = CH_3(g) + H(g)$			
Temperature (°C)	ΔH (kJ)	ΔS (J/K)	ΔG (kJ)
800.000	449.710	142.918	296.338
900.000	450.063	143.233	282.029
1000.000	450.251	143.388	267.697
1100.000	450.296	143.422	253.355
1200.000	450.208	143.361	239.015
1300.000	449.995	143.222	224.685

Figure S48. Data calculated from HSC Chemistry. HSC Chemistry is a software package including highly accurate thermochemical data; https://www.hsc-chemistry.com/

One notes that the ΔH values are almost invariant in Figure S48. Because of the large contribution to the translational entropy by having 2 gas phase species (CH_3 and H) on the right-hand side of the chemical equilibrium, and 1 gas phase species on the left-hand side (CH_4), comparing our calculated values of ΔG for *adsorbed* CH_4, CH_3, and H to the gas phase ΔG values, **inappropriately** favors this large ΔS_{trans} contribution in the gas phase. It is for this reason that we discuss our calculated **ΔH** values below so they can be compared to the 450 kJ/mol (i.e., 4.66 eV) gas phase ΔH value (Figure S48). Thus, it is the *change in endothermicity* due to the methane-liquid metal interaction that is relevant, by comparing our calculated $\Delta H_1 + \Delta H_2$ to the gas phase value ΔH = 4.66 eV.

The C-H bond dissociation (the sum of ΔH_1 and ΔH_2 is the relevant energy change) can *readily* occur on Ga atom, Ga-Ga dimer, Fe atom, or Ni atom: The calculated C-H bond dissociation enthalpy values ($\Delta H_1 + \Delta H_2$, Table R1) are 0.50 eV (Ga atom), -0.27 eV (Fe atom), 1.64 eV (Ni atom), and 0.51 eV (Ga-Ga dimer). All values are *much smaller* than the gas phase bond dissociation energy of ~4.66 eV. Indeed, the calculated change in endothermicity for the reaction when the methane is considered as 'adsorbed' to these species, is remarkable.

Of course, Ga, or Ga-Ga, (or Fe or Ni) would have Ga-Fe-Ni liquid metal 'beneath' them; to include (as best we could) the role of this LM on C-H bond dissociation for surface adsorbed CH_4, we made a periodic slab including Ga, Fe, and Ni atoms. A

Ga_9FeNi cluster was 'cut out' of the fully optimized periodic Ga slab surface (the '100' surface of alpha-gallium) that was doped by Fe and Ni atoms placed in interstitial sites. The Ga, and Ga-Ga, were then placed 'atop' this Ga_9FeNi cluster.

The Ga/Ga_9FeNi yielded a C-H dissociation enthalpy value of -0.11 eV and Ga-Ga/Ga_9FeNi a value of 2.75 eV. These values are also significantly lower than 4.66 eV. (We did not pursue Fe or Ni atop this Ga_9FeNi cluster due to computational complexity.)

Our computed values for gas phase methane being adsorbed and then converting to adsorbed methyl radical and adsorbed H atom radical show that the experimental liquid metal should be remarkably activating of methane at the temperatures around 1300 K used in experiments.

Table S3. Calculated CH_4 adsorption free energy (ΔG_1: $G(CH_4(ads)) - G(CH_4) - G(cluster)$) and bond dissociation energy of adsorbed CH_4 (ΔG_2: $G(CH_3(ads)) + G(H(ads)) - G(CH_4(ads))$) on different clusters. The $\Delta G_1 + \Delta G_2$ is the overall Gibbs free energy change of the reaction ($CH_4(g)$ + cluster → $CH_3(ads)$ + H(ads)). The change in enthalpy for each reaction is also shown, ΔH_1 and ΔH_2. All calculations were performed with Gaussian in which electronic energy was obtained by the MP2 method. Atom positions were kept fixed in Ga_9FeNi during optimization while Ga or Ga-Ga atop Ga_9FeNi were optimized. The temperature was set to 1300 K.

Reactant State	CH_4(ads)	CH_3(ads) + H(ads)	ΔG_1(eV) ΔH_1(eV)	ΔG_2(eV) ΔH_2(eV)	$\Delta G_1 + \Delta G_2$ (eV) $\Delta H_1 + \Delta H_2$ (eV)
Ga	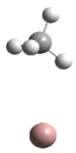	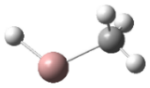	0.96 0.23	0.58 0.27	1.54 0.50
Fe		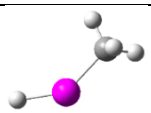	-0.60 -1.52	1.06 1.25	0.46 -0.27
Ni	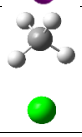	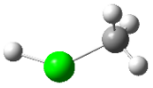	1.60 0.56	1.07 1.08	2.67 1.64
Ga	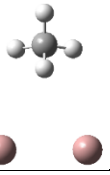	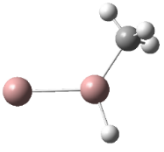	0.98 0.31	0.68 0.20	1.66 0.51

Ga 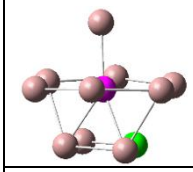	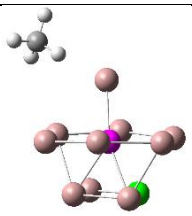	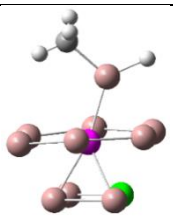	1.09 0.33	0.34 -0.44	1.43 -0.11
Ga-Ga 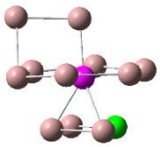	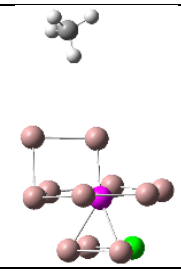	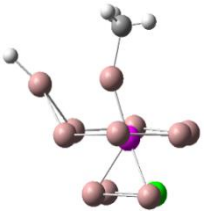	1.37 1.08	2.68 1.67	4.05 2.75

Table S4. Calculated electronic energy (E_e), zero-point energy (ZPE), entropy correction (-TS) and thermal correction (U), where Gibbs free energy was obtained via $G= E_e + ZPE – TS + U$. The unit is a.u. and the temperature was set to 1300 K.

Species	E_e	ZPE	-TS	U (thermal correction)	$G = E_e + ZPE –TS + U$
CH_4	-40.33408	0.04401	-0.14256	0.02287	-40.40975
Ga	-1923.14743	0	-0.09799	0.00617	-1923.23925
CH_4(ads) on Ga	-1963.47907	0.04447	-0.21365	0.03465	-1963.61360
CH_3(ads) + H(ads) on Ga	-1963.4655	0.03931	-0.20228	0.03629	-1963.5922
Fe	-1262.29547	0	-0.10048	0.00618	-1262.38977
CH_4(ads) on Fe	-1302.69165	0.04510	-0.20893	0.03404	-1302.82144
CH_3(ads) + H(ads) on Fe	-1302.6417	0.03787	-0.21578	0.03727	-1302.7823
Ni	-1506.80815	0	-0.09859	0.00618	-1506.90057
CH_4(ads) on Ni	-1547.12702	0.04420	-0.20286	0.03430	-1547.25136
CH_3(ads) + H(ads) on Ni	-1547.08396	0.03868	-0.20343	0.03664	-1547.2121
Ga-Ga	-3846.34048	0.00037	-0.15568	0.01406	-3846.48174
CH_4(ads) on Ga	-3886.67344	0.04499	-0.27343	0.04642	-3886.85546
CH_3(ads) + H(ads) on Ga-Ga	-3886.66291	0.04116	-0.25580	0.04722	-3886.83034

Ga/Ga_9FeNi	-22001.49460	0.00043	-0.24494	0.02426	-22001.7148
CH_4(ads) on Ga/Ga_9FeNi	-22041.8284	0.045113	-0.359966	0.058743	-22042.08451
CH_3(ads) + H(ads) on Ga/Ga_9FeNi	-22041.84116	0.04147	-0.33145	0.05911	-22042.07203
CH_3(ads) + H(ads) on Ga/Ga_9FeNi	-23924.79256	0.00136	-0.28110	0.035728	-23925.03657
CH_4(ads) on Ga-Ga/Ga_9FeNi	-23965.0992	0.04580	-0.41309	0.07049	-23965.3960
CH_3(ads) + H(ads) on Ga-Ga/Ga_9FeNi	-23965.03437	0.041873	-0.37633	0.07114	-23965.29769

Activation of methane by pure liquid gallium: experimental studies

Wi, et al., reported the activation energy E_A of 115.3 kJ/mol for the decomposition of CH_4 on an electrostatically levitated droplet of liquid gallium (E_A values for molten In, Sn, Bi, and Cu droplets are also reported)[8]. Ga is *much* more activating than Sn and Bi, and *significantly* more activating than In and Cu as well; 115.3 kJ/mol is much smaller than the enthalpy change for *CH_4 converting to CH_3 and H in the gas phase* at 1300 K of 450 kJ/mol (Fig. S48); and this obtained value of E_A = 115.3 kJ/mol is, of course, an *upper bound* on the enthalpy change for conversion of adsorbed methane on pure liquid gallium.

We note, also, the study by Fujita, et al[9], in which they fit rate data for the decomposition of methane, in their study of very low temperature growth of graphene onto the edges of pre-existing (~1 μm lateral dimension) graphene "seeds" on sapphire or polycarbonate surfaces. Quoting verbatim from their paper: "*The Arrhenius plot shows two temperature windows with distinct energy barriers, i.e., a high-temperature region >500 °C with an activation barrier E_a of ~0.58 eV and a low-temperature region <300 °C with an activation barrier E_a of ~0.16 eV. The window between 300 °C to 500 °C is a transition range in which processes associated with the two above barrier values are both contributing. The E_a ~0.58 eV barrier is consistent with the reported*

values from 0.52 eV to 0.77 eV obtained with a Ni catalyst. However, the observed low E_a ~0.16 eV for the low-temperature graphene edge growth is surprising. It suggests that a simple methane activation process is unlikely valid. Instead, parallel processes could be competing in the molten gallium catalyst, particularly at a lower temperature."

For the reader's convenience: 0.58 eV = 56 kJ/mol; 0.16 eV = 15 kJ/mol.

Note S2. Simulations about the role of Si.

To try to provide a theoretical understanding of possible initial steps towards diamond formation in the liquid metal used in experiments, *ab*-initio molecular dynamics (AIMD) and density functional theory (DFT) electronic structure analysis were performed. The formation energy per atom at the initial stage was calculated to help understand the process of clustering of carbon dissolved in liquid Ga (that we sometimes refer to as "the solvent" but also as "pure liquid gallium" in the text). The formation energy per atom was calculated as:

$$E_{\mathrm{Formation}} = (E_{n\mathrm{C}+m\mathrm{Si}+\mathrm{solvent}} - E_{\mathrm{solvent}} - n\mu_{\mathrm{C}} - m\mu_{\mathrm{Si}})/(n+m),$$

where n and m refer to the number of carbon and silicon atoms in the liquid metal solvent, and $E_{n\mathrm{C}+m\mathrm{Si}+\mathrm{solvent}}$, E_{solvent}, μ_{C}, and μ_{Si} indicate the *total energy of the solution*, the *energy of the solvent* (the liquid gallium), and the *chemical potential of C and Si*, respectively. The chemical potential of C and Si is the change in energy when each was added to the liquid gallium solvent, namely,

$$\mu_{\mathrm{C/Si}} = (E_{\mathrm{C/Si}} - E_{\mathrm{solvent}}).$$

Fig. S49a shows the formation energy of C_2, Si-C, Si-C-C, and C-Si-C per atom in two types of solvent, a *pure liquid Ga* and a liquid mixture of *120 Ga, 13 Ni, and 13 Fe atoms (denoted as Ga-Ni-Fe)*. For the pure liquid gallium case, each of C_2, Si-C, Si-C-C, and C-Si-C have a negative formation energy indicating these dimers or trimers are favored relative to the atomic species. For liquid Ga-Ni-Fe the formation energy was lowered from -0.37 to -0.63 for C_2, from -0.27 to -0.70 for Si-C-C, and from -0.09 to -0.73 for C-Si-C, in eV/atom; thus C_2, Si-C-C, and C-Si-C are substantially stabilized in liquid Ga-Ni-Fe. We note that Si-C was found to be dissociated at equilibrium in liquid

Ga-Ni-Fe, which is attributed to a stronger Fe-C interaction than Si-C.

Regarding the effect of Si, the electrostatic interaction was found to lower the formation energies of Si-C-C and C-Si-C from a Bader charge analysis, as shown in Fig. S49b.

The electronegativity of a C atom (χ_{C} =2.55) is higher than that of Ga, Ni, and Fe (χ_{Ga} =1.81, χ_{Ni} =1.91, and χ_{Fe} =1.83), and indeed in the liquid Ga at 1300 K the C atom has 0.97 more electrons on average than a neutral C atom. Si has an electronegativity (χ_{Si} =1.90) similar to that of Ga and the Bader analysis shows only a small change in the number of electrons compared to a neutral Si atom.

In the C_2 dimer, a C-C covalent bond is found and the interaction with liquid Ga was found to be smaller, so the number of additional electrons for each carbon atom is reduced by 0.3 to 0.4 compared to the isolated C atom. For Si-C, the interaction between Si and C is weak, so mostly it remained in dissociated form, thus the number of electrons is close to that of the atomic case. However, when a Si atom contacts *two* C atoms, this Si atom supplies additional electrons to the neighboring C atom. In Fig. S49b, Si in the C-Si-C structure loses 1.3 electrons on average, and the two C atoms have 11.07 electrons. In the structure Si-C-C, $C_{(1)}$ directly bonded to Si has 5.03 electrons, whereas $C_{(2)}$ that is the second neighbor of Si has 4.55 electrons which is similar to the average number of electrons of C_2 without Si. The electron transfer from Si to C *rationalizes* the significantly lowered formation energies of Si-C-C and C-Si-C.

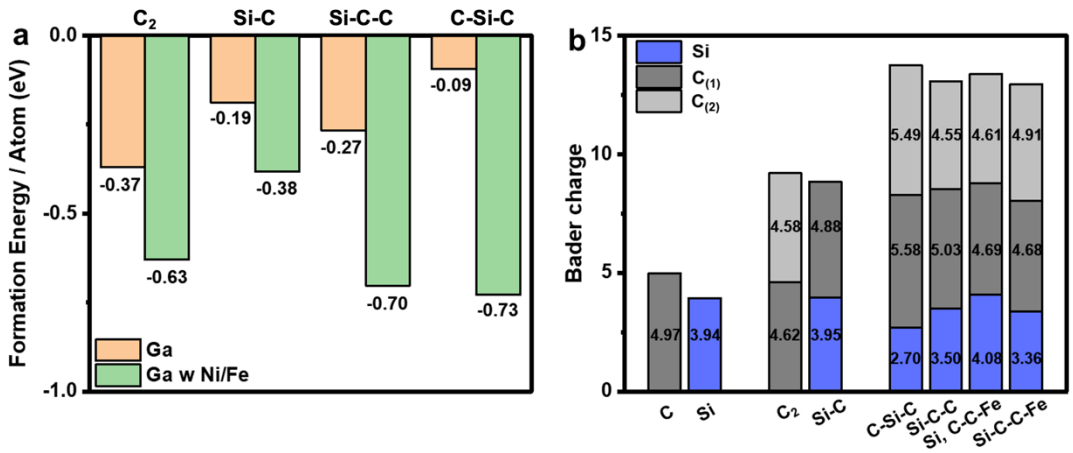

Figure S49. (a) Formation energy per atom in 120 Ga liquid metal (orange column) and in the Ga-Fe-Ni liquid metal (120 Ga, 13 Ni, and 13 Fe; green column). (b) The

Bader charge for each species in the Ga-Fe-Ni liquid metal.

In addition, the interactions of Fe with C as C moves around in the Ga-Fe-Ni liquid metal contributes to lower the formation energies of C_2, Si-C-C, and C-Si-C as shown in Fig. S49a. An image of each species within the Ga-Fe-Ni liquid metal and its relative total energy is shown in Fig. S50, and we found that those with an Fe-C interaction have relatively lower total energies compared to those without such a Fe-C interaction. And as mentioned the formation energy is further lowered by the presence of Si in the cluster, note the two values in Fig. S50 for Fe-C-C (-0.49 eV) and Fe-C-C-Si (-0.92 eV), respectively.

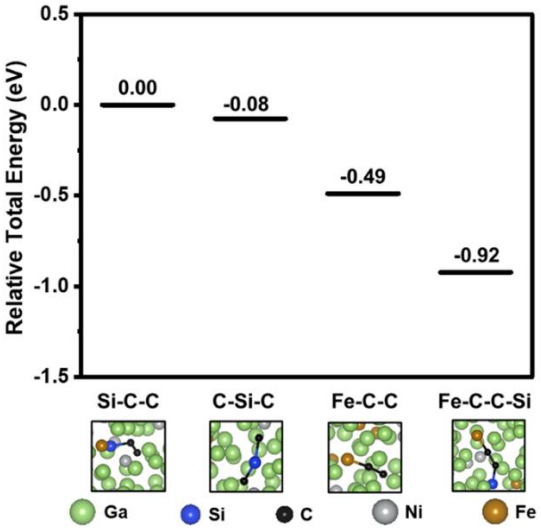

Figure S50. Relative total energies of Si-C-C, C-Si-C, Fe-C-C, and F-C-C-Si and their structures. There is one Si and two C in the Ga-Ni-Fe solvent in each case.

From our analysis of the formation energy and the Bader charge, a Si atom plays a special role in stabilizing such small clusters that are possibly the starting point of building larger clusters (this is discussed below) and finally, diamond nuclei.

Projected density of states (PDOS) analysis was done to further understand the formation energies and Bader charges (Fig. S51). Both C and Si atoms dissolve in liquid gallium, a metal having zero band gap and showing free electron behavior. In the C atom, the s-orbital maintained the local atomic state in the low energy region below -10 eV compared to the Fermi level, whereas the s-orbital of Si was also assimilated to the state of Ga and became broader like the p-orbital of Si. In addition, the projected

DOS of the isolated single C atom and the C_2 dimer differed in s-orbital character in the low energy region. The C_2 dimer has a stable C-C covalent bond state around -15 eV relative to the Fermi level, and these states lower the C_2 formation energy. As mentioned above, in terms of formation energy, Si showed greater stability when connected to two C atoms than when interacting with a single C atom, and the projected DOS results also support this. The bond between Si and a single C atom was weak, and the orbital overlap was minimal. When Si is connected to two C atoms (Si-C-C, C-Si-C), the orbital overlap is greatly improved through the formation of a bond with C in the low energy region. Compared to the C-C bond state of the C_2 dimer, the energy level of the carbon bonding state of Si-C-C moved to a lower value.

This is the reason why Si strengthened the C-C bond and the Si-C-C structure has a significantly lower formation energy. The projected DOS of the Fe-C-C and Fe-C-C-Si structures show that the interaction between Fe and C is related to the p-orbital around -1 eV compared to the Fermi level. The gray area in Fig. S51g-h shows that the C in direct contact with Fe overlaps with the states of Fe, slightly increasing the p-orbital DOS. Among other MD simulations, there was a case where C was surrounded by transition metals, and the p-orbital of C, which was broad (highly delocalized “into” the surrounding liquid gallium) due to interaction with the neighboring Ga atoms; in this case of neighboring Fe and Ni atoms as well as Ga atoms, we find a fairly high peak and local properties (Fig. S52). This result also indicates that Fe and Ni (and likely some of the other transition metals, such as Co) mainly interact with the p-orbital of C for a liquid metal mixture composed of 120 Ga, 13 Fe, and 13 Ni atoms.

To study the role Si plays, a moderately large number of C atoms were dissolved in the liquid Ga-Fe-Ni with and without Si atoms, and the MD trajectories were studied. For no Si, the unit cell in the slab model contains 120 Ga, 13 Ni, 13 Fe, and 15 C, and in the first part of the MD trajectory of 18 ps (Supplementary Movie 1), C_3 was the largest size of C cluster formed. We then added another 5 C atoms (making 20 C in total) and performed a second MD of 16 ps (Supplementary Movie 2). Likewise, in the presence of Si, a first MD of 15ps was performed with 15 C and 5 Si atoms dissolved in the Ga-Ni-Fe liquid metal (Supplementary Movie 3), and after adding 5 more C

atoms, an additional MD of 16ps was then done (Supplementary Movie 4). In the case without Si, no carbon structure larger than C_3 was found in both the first and second runs of MD (Supplementary Movie 1 and 2, Figure S53a). However, in the presence of Si atoms, Si-C-C, C-Si-C, and C3 structures were formed in the initial MD, and after additional C atoms were supplied, a cluster containing tetrahedral Si and multiple carbon atoms was formed within 10 ps (Fig. S53b) and stabilized a carbon cluster (Supplementary Movie 4, Fig. S53c).

PDOS were obtained for the final structures of MD in the presence and absence of Si, respectively (Fig. S54a-b). When there is no Si, electronic states corresponding to several C_2 dimers or C_3 chains appeared (Fig. S54a), and in the Ga-Fe-Ni liquid metal with Si atoms, many bonding states appeared between Si and C (Fig. S54b). In particular, the p-orbital state of carbon between -10 and -5 eV increased due to the influence of Si; this means that the p-orbitals of the carbon cluster are localized in that energy level. In addition, the observed tetrahedral Si showed an electronic state close to sp^3, showing formation of this sp^3-bonded when Si atoms are present (Fig. S54c).

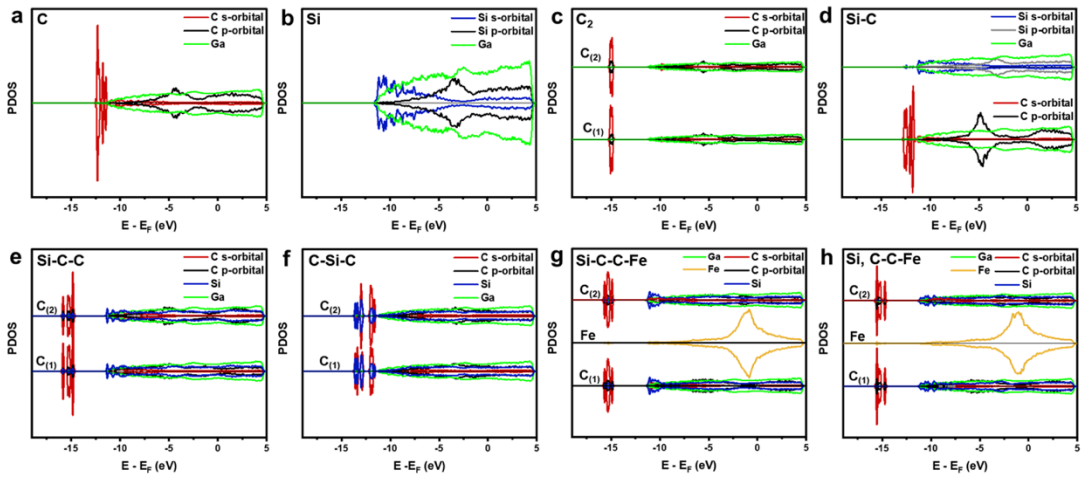

Figure S51. Projected DOS of the indicated clusters. (a-b) PDOS for a single atom in Ga-Ni-Fe solvent: (a) C and (b) Si. (c-d) PDOS is presented for: (c) C_2 and (d) Si-C. (e-h) PDOS of (e) Si-C-C, (f) C-Si-C, (g) Si-C-C-Fe, and (h) C-C-Fe (with isolated Si). The s-orbital and p-orbital of carbon are shown in brown and black, respectively. In (b) and (d), the s-orbital and p-orbital states of Si are shown in blue and gray, respectively, but in (e), (f), (g), and (h), the Si state is shown in blue. In a two-carbon structure, the first carbon is denoted as $C_{(1)}$ and the second carbon is denoted as $C_{(2)}$, respectively, and the Fe state bonded to carbon is shown in orange in (g) and (h). The gray area in (g) and

(h) shows the states where Fe and C overlap and form bonding states. PDOS is the result of summing each element type and dividing by the number of elements.

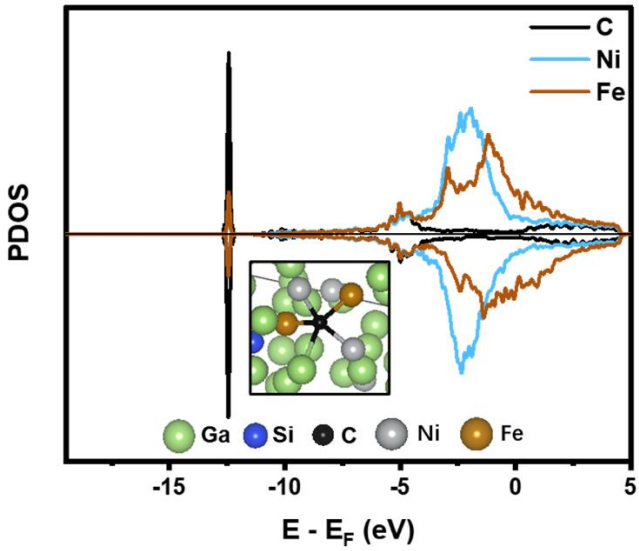

Figure S52. Projected DOS and its structure when carbon interacts with many surrounding Ni and Fe atoms.

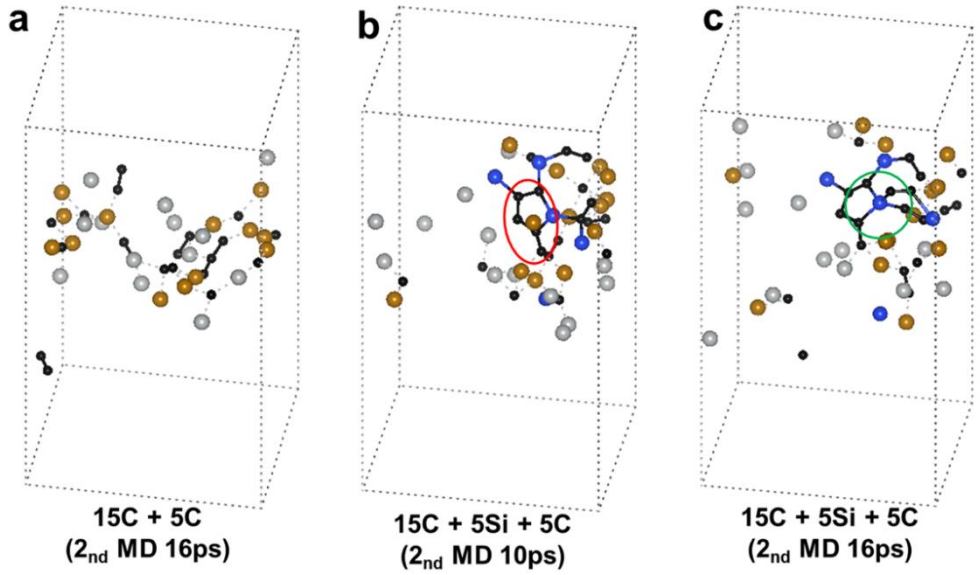

Figure S53. (a) The structure of the solute is shown by excluding the 120 Ga in the slab structure of the Ga-Fe-Ni liquid metal obtained after 18 ps of MD with 15 C atoms and then the 2nd MD of 16 ps by adding 5 more C atoms. There are no carbon clusters larger than C_3. (b-c) Structure in which (b) 10 ps (1st MD of 5 Si and 15 C) and then (c) 16 additional ps in the second MD in which 5 more C atoms were after the 1st MD (of 5 Si and 15 C). The biggest carbon cluster and tetrahedral Si is denoted by red and green circle, respectively.

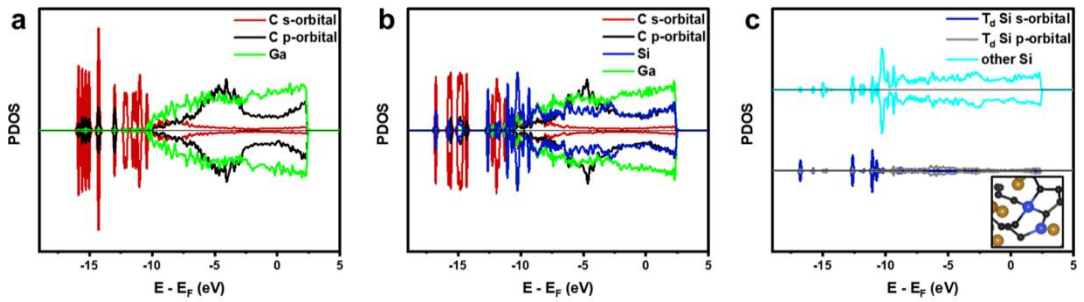

Figure S54. (a) PDOS of the structure shown in Fig. S53a. (b) PDOS of the structure shown in Fig. S53c. The colors used in (a) and (b) are the same as Fig. S51. (c) PDOS of tetrahedral Si surrounded by 4 C atoms (blue and gray indicate Si s- and p-orbital) and PDOS of the other Si (light blue). PDOS is the result of summing each element type and dividing by the number of elements.

In an attempt to test whether Si plays a role in maintaining sp^3-bonding of carbon clusters at some C cluster size, we embedded a diamondoid-like structure (however, with no C-H bonds present) in a pure liquid Ga slab and examined its structural deformation up to 10 ps of 1300 K AIMD. We chose adamantane, $C_{10}H_{16}$, and studied the deformation of the C_{10} core unit with no H's attached, and also a Si_6C_4 cluster in which 6 C's in this C_{10} core unit were replaced with Si; and finally, also clusters in which 1 C atom, or 6 C atoms, were added to Si_6C_4.

Fig. S55 shows each initial and final structure, and the 10 ps MD trajectory is shown in Supplementary Movie 5-8. The C_{10} structure *completely lost* its sp^3-bonding character and transformed into a chain within 5 ps (Fig. S55a). The Si_6C_4 structure maintained tetrahedral bonding of C to a large extent, i.e., the sp^3-bonding character was maintained relatively well (Fig. S55b). Upon addition of 1 or 6 C atoms to Si_6C_4, it was not deformed into a chain shape (Fig. S55c-d) and tetrahedral bonding persisted. Fig. S56 shows the projected DOS of the initial C_{10}, of the final chain shape C_{10}, and of the Si_6C_4 structure. The C_{10} cluster was thus not stable and indeed has fewer states, with the integration of states in the low energy region shown in gray being 4.03 (Fig. S56a); the C_{10} chain has more states, with the integration of states in the same energy region being 4.98 (Fig. S56b). Chain structures are preferred because they have more states in the lower energy region. In Si_6C_4, a stable cluster structure can be maintained because the integral value of the carbon state in the same energy region was 6.27 (Fig.

S56c).

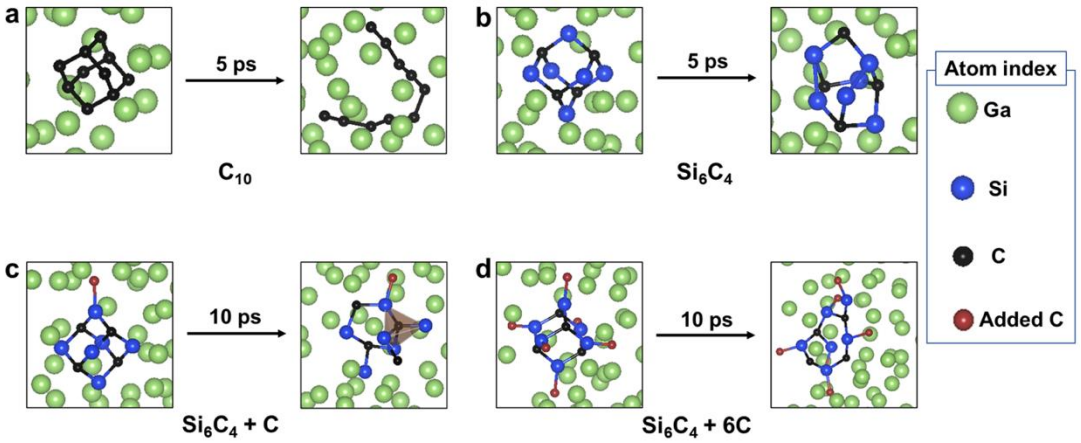

Figure S55. (a) Structure before and after 5 ps MD in liquid Ga of C_{10} structure with all hydrogen removed from adamantane, the smallest diamondoid. (b) 5ps MD results of a structure in which 6 C atoms are replaced with Si in H-free adamantane (thus, Si_6C_4). (c-d) Structures after 10ps, starting from (c) 1 and (d) 6 C atoms were added to the Si_6C_4 structure. In (c) and (d), the added C atoms are shown in brown color.

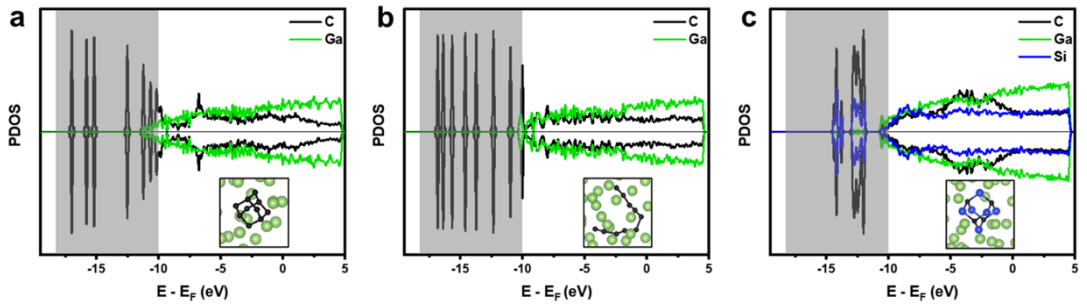

Figure S56. (a-c) PDOS of (a) The C_{10} cluster described in the text, (b) the C_{10} chain that forms, and (c) Si_6C_4. The states of C and Si are shown in black and blue, respectively, and Ga is shown in green.

Our theoretical calculations about the role(s) of Si strongly suggest Si can promote cluster formation (that could be called 'pre-nuclei', as we expect the nucleus to contain (roughly) 20 to 40 C atoms, and one or several Si atoms) with mostly sp^3-like C bonding, in liquid Ga.

Per our modeling at the experimentally relevant temperature of 1300 K, Si has three major roles: 1) C-C bond stabilization, 2) diamond pre-nuclei initialization, and 3) maintenance of sp^3-bonding character. For Si-C-C the calculated formation energy, Bader charges, and projected DOS show that Si makes the C-C bond stable. In the

presence of Si, tetrahedral C can be maintained and a plausible path to diamond nucleation is established in relatively small clusters Si_xC_y. As noted, Si helps maintaining C sp^3-bonding and we find that with Si present, C chains or C chains with Si atoms embedded in such hypothetical chains, *do not form*. But they readily form without Si.

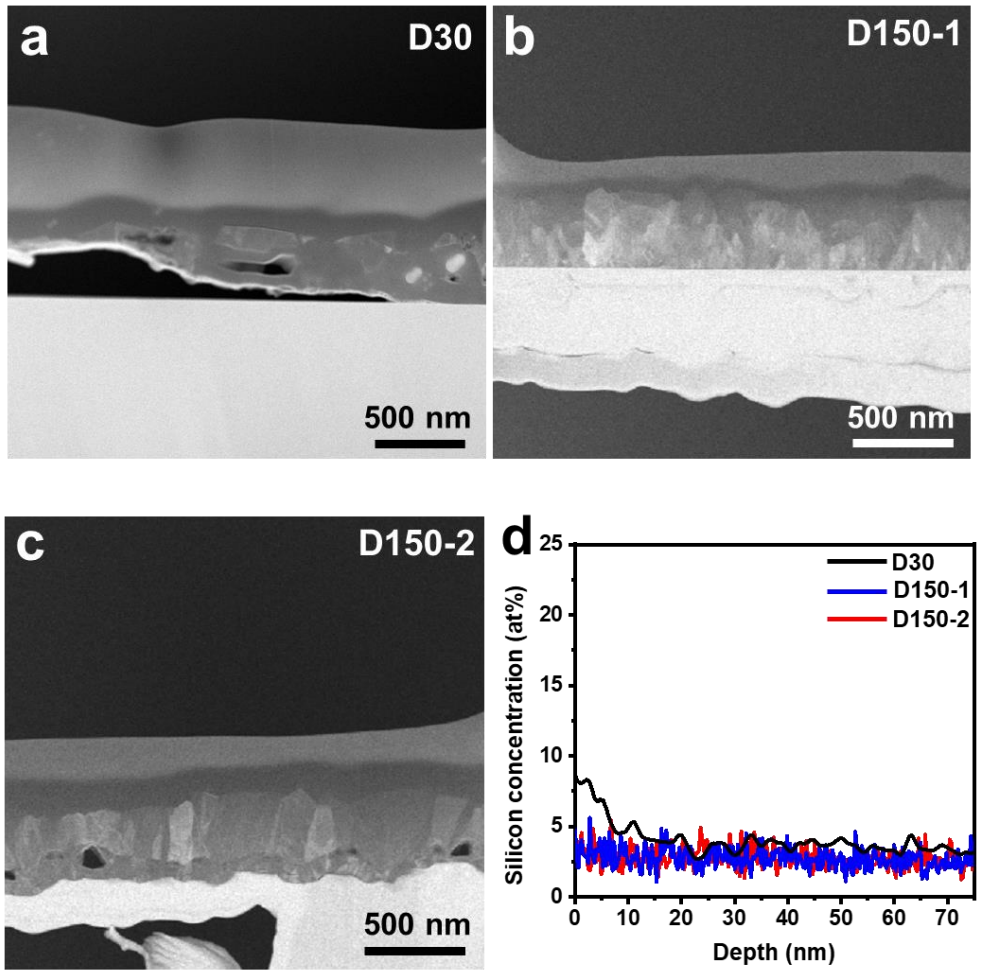

Figure S57. **TEM-EDS line profiling showing silicon concentration with depth.** (a-c) TEM images of D30 (this figure was used in Fig. 3g), D150-1 (this figure was used in Fig. 3a) and D150-2 (this figure was used in Fig. S38). (d) TEM-EDS line profiling showing silicon concentration at different depths of D30, D150-1, D150-2.

We found that the carbon rich M1 region is also silicon rich for the sample obtained for an early stage of growth (D30). The silicon concentration decreases from ~8.6 at% at the top surface of M1 region to ~4.0 at% at a depth of ~20 nm. And, the M1 regions in the sample after a growth run of 150 min show a significant reduction of the amounts of silicon in the subsurface regions, for both the M1 region that is contacting the diamond film (D150-1) and the M1 region that is contacting with the graphite film (D150-2). This suggests that silicon in the subsurface regions is consumed as diamond grows.

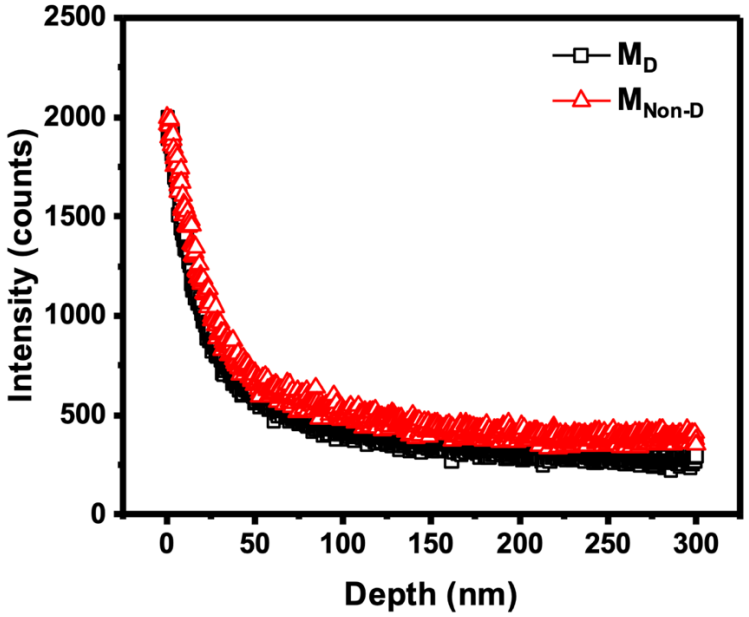

Figure S58. ToF SIMS depth-profiling of silicon concentrations (ion counts as function of the depth from the surface) obtained on two different regions of the solidified liquid metal pieces.

We further studied the distribution of Si in the subsurface regions of the solidified liquid metal (optimized condition, after growth of diamonds for 150 min) by using ToF-SIMS depth-profiling (Fig. S58). The regions underneath the as-grown diamonds, and the regions without diamond formed at the surface, were both studied. We note that there are certain amounts of Si found in both regions, and the concentration of Si decreases with increasing depth and reaches constant intensity (ion counts of ~350) when the depth is about 100 nm.

The concentration of Si in the subsurface regions (e.g., M1 region) of liquid metal correlates closely with the growth of diamonds. When Si was consumed (such as by forming SiV^- color centers in the as-grown diamonds) such that the concentration of Si in M1 region is decreased to some extent, growth of diamonds stops, though there were certain amounts of Si present in the solidified liquid metal bulk.

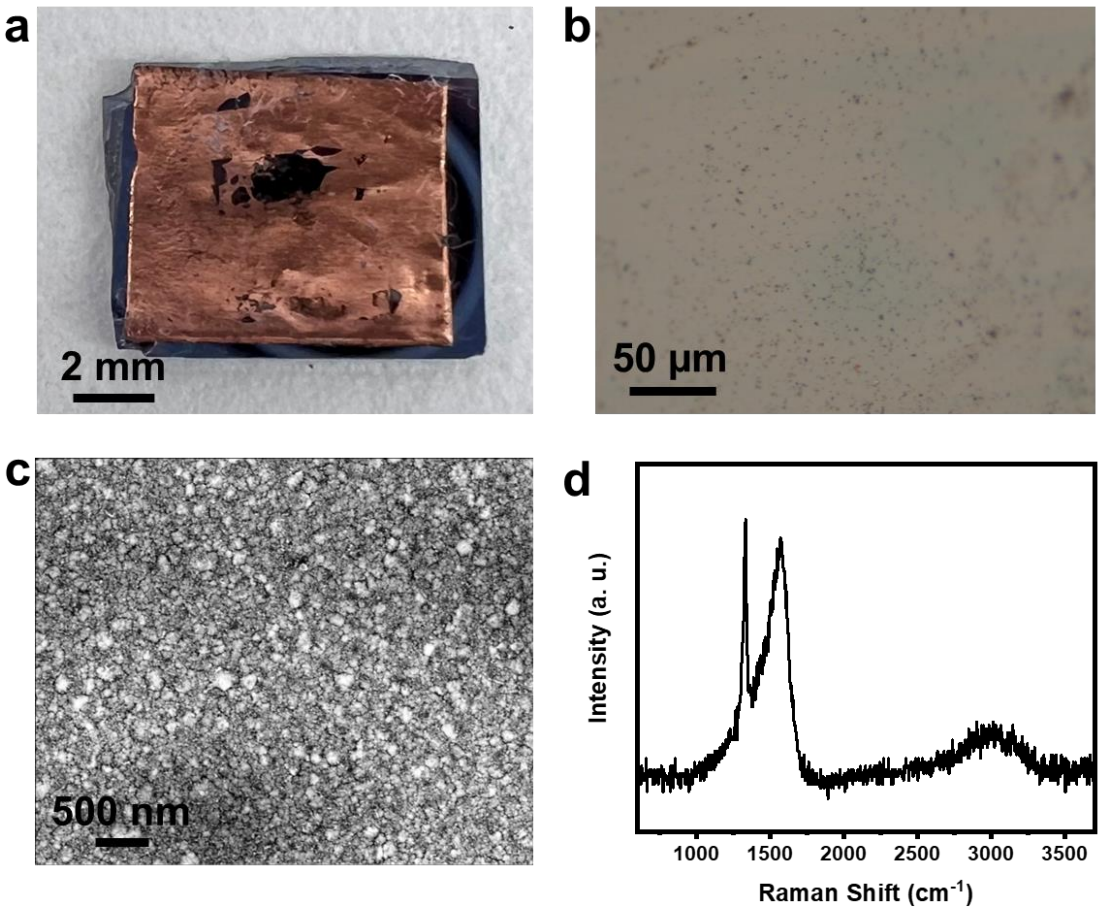

Figure S59. The growth result for the liquid metal composed of 0.25 at% Si, 14.67 at% Ni, 7.33 at% Fe, 38.87 at% In and 38.88 at% Ga. The photograph (a), optical microscope image (b), SEM image (c) and UV raman spectrum of as-grown diamond film transferred by Cu tape that was "sticked onto" the silicon wafer.

We used $Ga_{38.88}/In_{38.87}/Ni_{14.67}/Fe_{7.33}/Si_{0.25}$ for a growth run, and found a homogenous liquid alloy was formed at the growth temperature. A 'transparent but dark' film was observed on the solidified liquid metal surface (adjacent to the EDM-3 Poco graphite sheet piece). This film was delaminated by using a double-side copper tape and transferred onto a 300 nm SiO_2/Si wafer substrate (Fig. S59a-b). This film is a diamond film per UV Raman spectroscopy (Fig. S59d), but the quality of the film (showing a very intense graphite G band) is a bit worse compared to our typical growth using Ga/Ni/Fe/Si. The facets were also not clear (Fig. S59c).

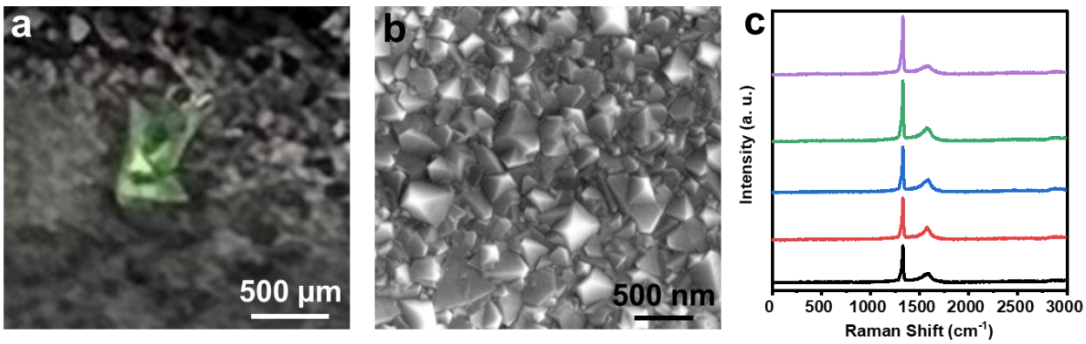

Figure S60. (a) A photograph (note green colored region), (b) an SEM image, and (c) Raman spectra: of the as-grown diamond film found on the solidified liquid metal surface. The Ga/Co/Fe/Si growth run: 760 Torr, 1175 °C, 150 min, 73.75 at% Ga, 15.00 at% Co, 11.00 at% Fe, 0.25 at% Si.

A polycrystalline diamond film was grown by using a liquid metal containing Ga, Co, Fe, and Si. The morphology of the diamond film is similar to that grown by using the liquid metals containing Ga, Co, Fe, and Si (Fig. S60b; and see main text). Raman spectra (Fig. S60c) from randomly selected regions over the green region in Fig S60a confirmed it is diamond.

Note S3. More details about the graphite crucible and EDM-3 Poco Graphite.

Are small particles of diamond or DLC carbon being deposited from the machining of our graphite crucibles? The graphite crucible is machined from IBIDEN EX-60 graphite (obtained by the company in Korea that machined these crucibles, GPMI, from IBIDEN Graphite Co., Ltd, Japan). An internet search readily shows that, e.g., 'isotropic graphites' can be dry machined with carbide tools that are coated with a film of 'DLC' (diamond-like carbon) that, it is said, provides the tool with better wear. However, GPMI did not use such tool bits in machining our crucibles, instead they used tungsten carbide tool bits from Royal Corp. Thus, diamond particles or DLC particles, are *not* present in our crucible (cavity) due to wear of a DLC-coated carbide tool because such DLC-coated tools were not used in machining (preparing) our crucibles.

Are small particles of diamond or DLC carbon present due to the dry machining step? Our search of the literature finds no reference (to the best of our knowledge) of the formation of diamond particles or DLC-like particles, due to machining of graphite.

How small can diamond particles be and still yield Raman spectra? We note the UV-Raman of 1-nm diamond particles have been obtained in a relatively pure nanodiamond sample of particles in that size range[10].

Raman spectroscopy was used to study *the machined graphite at the bottom of the crucible cavity that was 'machined into' IBIDEN EX-60 graphite,* and *the EDM-3 Poco Graphite sheet*, before and after annealing at 1100 ºC in a gas flow of H_2(g) and Ar (Ar(g): H_2(g) ratio is 1:5) at a pressure of 1 atm for 8 h. We found that the graphite crucible after annealing shows a much more intense D band (with a D band to G band intensity ratio about 2x larger) than of the as-received one, and the Raman spectra of the EDM-3 Poco Graphite did not change, with essentially identical D band to G band intensity ratio, for before and after annealing (Fig. S61a-f). Such an increase of D band might be due to metal-impurity-mediated H_2 etching of the graphitic structures[11-14]. More importantly, we did not find evidence for any diamonds in either the as-received or the annealed graphite crucible, or the as-received or annealed EDM-3 Poco Graphite (Fig. S61g-h).

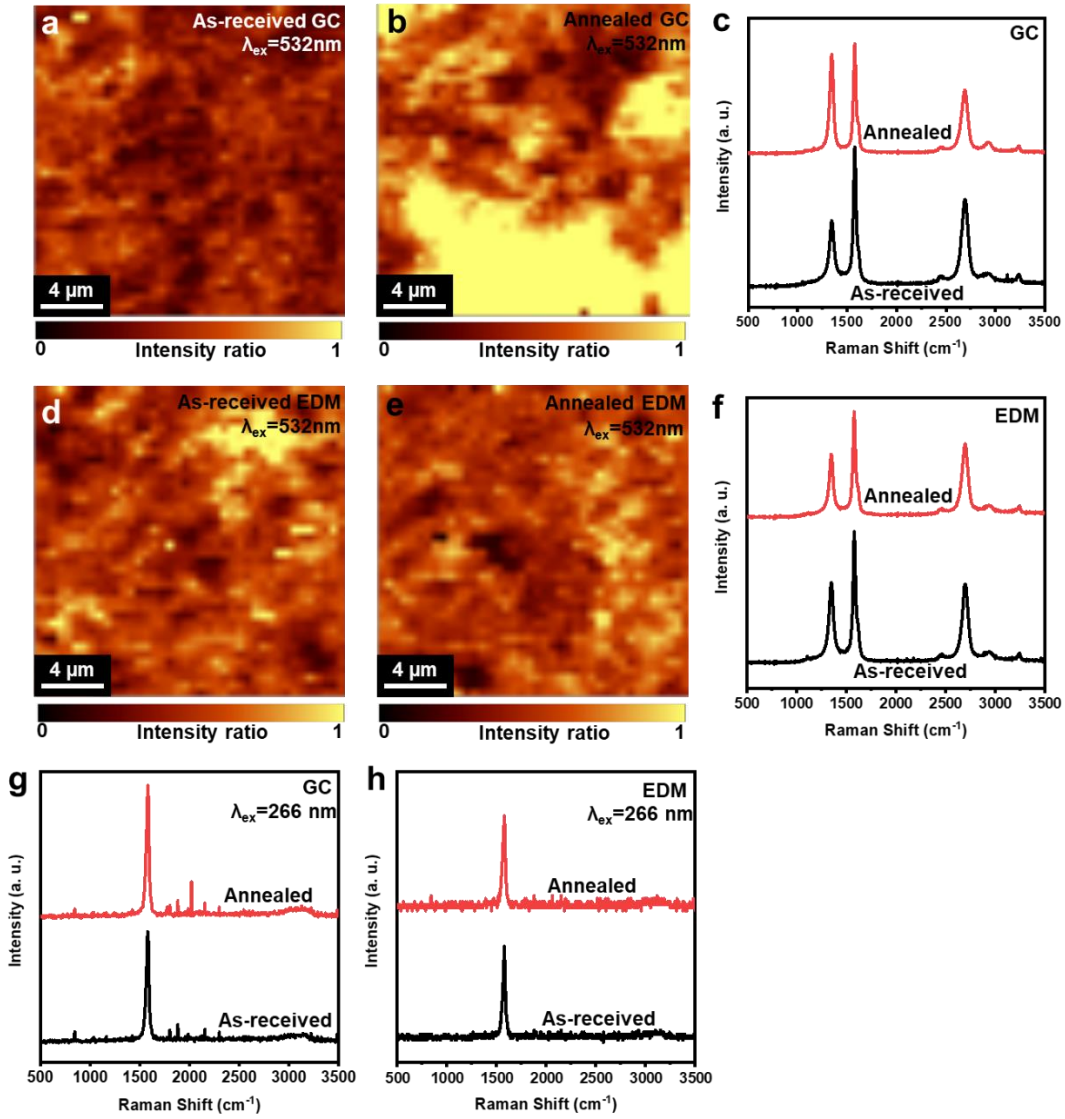

Figure S61. Raman spectroscopy of graphite crucible (GC, 'cavity bottom surface') and EDM-3 Poco Graphite (EDM). Note: (a-f) were obtained with a 532 nm laser. (g, h) were obtained with a 266 nm laser. (a-b) Raman maps of the intensity ratio of the D band to G band of the (a) as-received GC, and (b) GC after annealing. (c) Averaged Raman spectra obtained from the entire mapped regions of (a) and (b). (d-e) Raman maps of D band to G band intensity ratio of the (d) as-received EDM, and (b) EDM after annealing. (f) Averaged Raman spectra obtained from the entire mapped regions of (d) and (e). (g-h) UV Raman spectra of (g) GC and (h) EDM before and after annealing.

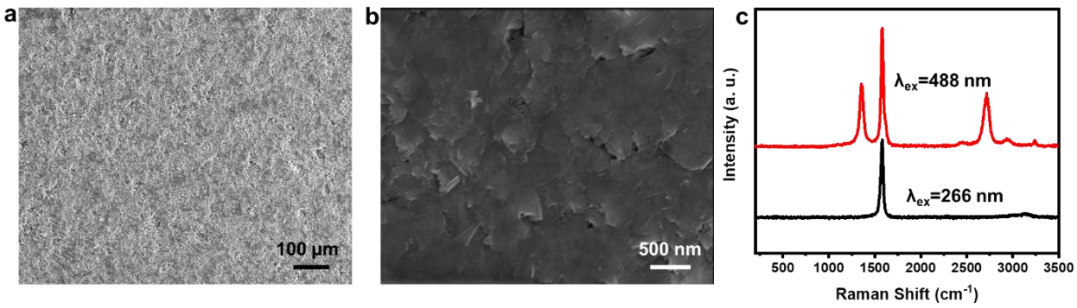

Figure S62. The experiment without liquid metal. (a) The low magnification SEM image and (b) the high magnification SEM image of graphite crucible after running experiment. (c) The Raman spectra obtained by 266 nm and 488 nm.

We have heated an empty graphite crucible to 1175 ºC (the temperature of the crucible wall reading by pyrometer) under 760 Torr of methane/hydrogen at a molar ratio of 1/20 for 150 min. Our SEM and Raman studies of the crucible bottom surface show that there no diamonds grown (Fig. S62; We note that we extensively explored many regions of the crucible bottom surface by both SEM and Raman.) Thus, the liquid metal use is critical for the growth of diamonds.

References

1 Thoms, B. D., Pehrsson, P. E. & Butler, J. E. A vibrational study of the adsorption and desorption of hydrogen on polycrystalline diamond. *Journal of Applied Physics* **75**, 1804-1810, doi:10.1063/1.356373 %J Journal of Applied Physics (1994).

2 Ushizawa, K. *et al.* Surface-enhanced Raman spectroscopic study of hydrogen and deuterium chemisorption on diamond (111) and (100) surfaces. *Physical Review B* **60**, R5165-R5168, doi:10.1103/PhysRevB.60.R5165 (1999).

3 Luo, K. *et al.* Coherent interfaces govern direct transformation from graphite to diamond. *Nature* **607**, 486-491, doi:10.1038/s41586-022-04863-2 (2022).

4 Jiang, M. *et al.* Diamond formation mechanism in chemical vapor deposition. *Proceedings of the National Academy of Sciences* **119**, e2201451119, doi:doi:10.1073/pnas.2201451119 (2022).

5 Tulić, S. *et al.* Covalent Diamond–Graphite Bonding: Mechanism of Catalytic Transformation. *ACS Nano* **13**, 4621-4630, doi:10.1021/acsnano.9b00692 (2019).

6 Jin, S. *et al.* Colossal grain growth yields single-crystal metal foils by contact-free annealing. *Science* **362**, 1021-1025, doi:doi:10.1126/science.aao3373 (2018).

7 Ohtsuka, Y. *et al.* Theoretical Study on the C–H Activation of Methane by Liquid Metal Indium: Catalytic Activity of Small Indium Clusters. *The Journal of Physical Chemistry A* **123**, 8907-8912, doi:10.1021/acs.jpca.9b06374 (2019).

8 Wi, T.-G., Park, Y.-J., Lee, U. & Kang, Y.-B. Methane pyrolysis rate measurement using electromagnetic levitation techniques for turquoise hydrogen production: Liquid In, Ga, Bi, Sn, and Cu as catalysts. *Chemical Engineering Journal* **460**, 141558, doi:https://doi.org/10.1016/j.cej.2023.141558 (2023).

9 Fujita, J.-i. *et al.* Near room temperature chemical vapor deposition of graphene with diluted methane and molten gallium catalyst. *Scientific Reports* **7**, 12371, doi:10.1038/s41598-017-12380-w (2017).

10 Stehlik, S. *et al.* Size and Purity Control of HPHT Nanodiamonds down to 1 nm. *The Journal of Physical Chemistry C* **119**, 27708-27720, doi:10.1021/acs.jpcc.5b05259 (2015).

11 McKee, D. W. Effect of metallic impurities on the gasification of graphite in water vapor and hydrogen. *Carbon* **12**, 453-464, doi:https://doi.org/10.1016/0008-6223(74)90011-6 (1974).

12 Keep, C. W., Terry, S. & Wells, M. Studies of the nickel-catalyzed hydrogenation of graphite. *Journal of Catalysis* **66**, 451-462, doi:https://doi.org/10.1016/0021-9517(80)90047-0 (1980).

13 Lukas, M. *et al.* Catalytic subsurface etching of nanoscale channels in graphite. *Nature Communications* **4**, 1379, doi:10.1038/ncomms2399 (2013).

14 Cheng, G., Calizo, I., Hacker, C. A., Richter, C. A. & Hight Walker, A. R. Fe-catalyzed etching of exfoliated graphite through carbon hydrogenation. *Carbon* **96**, 311-315, doi:https://doi.org/10.1016/j.carbon.2015.09.079 (2016).